Brillouin Light Scattering Studies of Transition Metal Dichalcogenides MoS_2, $MoSe_2$, and WS_2

by

©Ameera Alrashdi

A Thesis submitted to the School of Graduate Studies in partial fulfillment of the requirements for the degree of

M.Sc.

Department of Physics and Physical Oceanography
Memorial University of Newfoundland

Memorial University of Newfoundland

July 2016

St. John's Newfoundland

Abstract

Brillouin Light Scattering has been used for the first time to probe surface and bullk acoustic phonons in the transition metal dichalcogenides MoS_2, $MoSe_2$ and WS_2. Rayleigh surface and transverse bulk acoustic phonon velocities were obtained from the Brillouin peak frequency shifts. Rayleigh velocities were 1690 ± 70 m/s, 1630 ± 40 m/s, and 1430 ± 50 m/s for MoS_2, $MoSe_2$, and WS_2, respectively. The Rayleigh surface phonon velocities are similar to those found for other transition metal dichalcogenides. The transverse bulk acoustic modes propagating approximately along the z direction, were observed for WS_2 and for MoS_2 and were calculated by measuring the average value of the frequency shift. The transverse velocities were found to be 2430 ± 70 m/s and 3450 ± 100 m/s, respectively. The bulk transverse velocities for MoS_2, and WS_2 were found to be $\sim$ 21 % and $\sim$ 44 % lower, respectively, than those of single layer samples determined using first-principle calculations. Moreover, from transverse acoustic phonon velocities the elastic constants, C_{44} was determined as 44 ± 1 GPa and 60 ± 3 GPa for WS_2, and MoS_2, respectively. In general, obtained elastic constants are higher than those obtained from other bulk and single layer studies.

Also, Brillouin peaks due to bulk modes were not seen for either sample of $MoSe_2$ so it was not possible to obtain the bulk velocities and elastic constants for this material. The extinction coefficient for $MoSe_2$ is much larger than those for WS_2 and MoS_2. This could be the reason why no bulk mode was observed in the Brillouin

spectra of $MoSe_2$.

Acknowledgements

I would like to express my gratitude to my supervisor Dr. Todd Andrews for all his help and support.

I should also appreciate my family, specially my husband Mr. Khalid Alrasheedi, for their patience and supporting moments. Without their help and their assurance this work could not ever be done.

I also like to thank my dear friends Mona and Somayeh for our happy moments, when I really needed to feel I am still alive.

At the end, I should thank the Department of the Physics and Physical Oceanography for using the lab instruments and the Ministry of Higher Education in the Kingdom of Saudi Arabia for the scholarship I have been granted.

Table of Contents

List of Tables

List of Figures

List of Abbreviations and Symbols

A	aperture
ω_i	angular frequencies of the incident light
ω_s	angular frequency of scattered photon
ω	angular frequency of acoustic phonon
ω_B	angular frequency of a bulk phonon
ω_R	angular frequency of Rayleigh surface phonon
θ_i	angle of incidence
θ_s	angle that the wave vector of scattered light make with the surface normal
BSP	beam splitter
BLS	Brillouin light scattering
DFT	density functional theory
F	filter
FSR	free spectral range
HWP	half wave plate
L	lens
M	mirror
$MoSe_2$	molybdenum diselenide
MoS_2	molybdenum disulfide
P	prism

QT	quasi-transverse bulk mode
QL	quasi-longitudinal bulk mode
R	Rayleigh surface mode peak
TMDCs	transition metal dichalcogenides
WS_2	tungsten disulphide
TFP	tandem Fabry-Perot interferometer
VNDF	variable neutral density filter
$\vec{k}$	wavevector of acoustic phonon
$\vec{k_i}$	wavevector of incident
$\vec{k_s}$	wavevector of scattered photon

Chapter 1

Introduction

1.1 Transition Metal Dichalcogenides Overview

Transition-metal dichalcogenides (TMDCs) are materials that have attracted considerable attention due to their unique structural, optical, elastic, and electronic properties. TMDCs are materials of the form of MX_2 that have a transition metal M, such as elements of groups IV (Ti, Zr, Hf), V (V, Nb, Ta) and VI (Mo, W) of the periodic table of the elements, and a chalcogen X (S, Se, Te), elements located in group XVI of the periodic table [5]. TMDCs are composed of many layers in which a transition metal layer is sandwiched between two chalcogen layers, and they are held together by weak van der Waals forces [6]. Each layer has hexagonal lattice structure [5]. The nature of the van der Waals forces makes it easy to cleave the planes [7]. However, the atoms within each layer are held strongly together by ionic-covalent bonding [6].

TMDCs exhibit packing polymorphism. In the bulk, TMDCs can be crystallized with three different stacking structures. These structures are classified as: 1T, tetragonal symmetry and octahedral coordination; 2H, hexagonal closed packing and trigonal prismatic coordination; and 3R, rhombohedral symmetry (see Figure 1.1) [8].

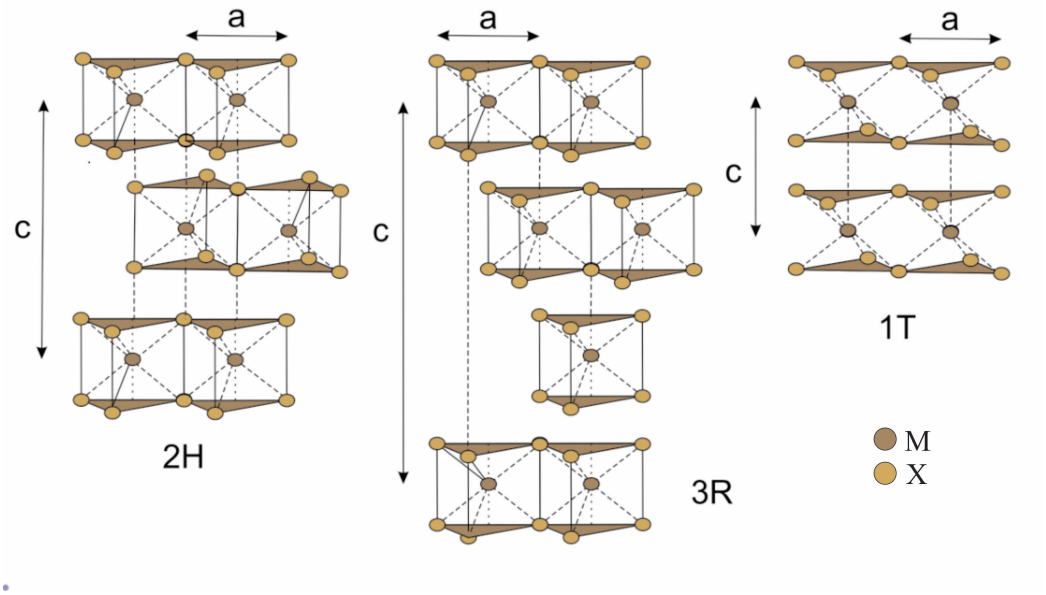

Figure 1.1: Different structures of transition metal dichalcogenides.

Due to a very small band gap, TMDCs have become attractive materials in physics like graphene and boron nitride [9]. Most semiconducting TMDCs have exhibited a transition from an indirect band gap at the Γ point to a direct band gap at the K point of the Brillouin zone when their thicknesses are reduced to a single layer. The band gap in most semiconducting TMDCs, both in bulk and monolayer, are comparable to the 1.1-eV gap for silicon [8]. Due to their interesting band gap transformation, TMDCs are favorable for solar cells and many electronic applications, like nanoscale field-effect transistors [10]. The ability of these materials to absorb and emit light are strongly affected by the electronic band structures [8].

In 2D TMDCs layers, transport and scattering of the carriers are confined to the

plane of the material. The mobility of carriers is affected by different scattering mechanisms, which are also seen in other semiconductors like graphene [11]. The carrier mobility is dependent on the layer thickness, carrier density, temperature, effective carrier mass, electronic band structure and phonon band structure [4]. Moreover, the large Young's modulus of single-layer and multi-layer dichalcogenides sheets make them attractive semiconductors for flexible electronic and optoelectronic devices, as well as for composite films [12].

The properties of TMDCs materials are unique and their applications are relatively new, and it is expanding the area of research rapidly. In this work, we focused on studying the elastic properties of the three TMDCs: molybdenum disulfide (MoS_2), molybdenum diselenide ($MoSe_2$), and tungsten disulphide (WS_2).

MoS_2 is one of the interesting family members of TMDCs due to its distinctive electronic, optical, and catalytic properties. For example, it can be used as a hydrodesulfurization catalyst, or a photocatalyst [13]. MoS_2 is used in photovoltaic cells, nanotribology, lithium batteries, and the dry lubrication industry [14]. MoS_2 has two different structures. The first one is 2H-MoS_2, while the second one is 3R-MoS_2. Both structures have the trigonal prismatic coordination [15]. The 3R-MoS_2 is less dominant and stable in nature; and it transforms to 2H-MoS_2 upon heating [16]. Monolayer MoS_2 is a direct band gap semiconductor and the photoluminescence intensity increases drastically with decreasing number of layers to one [17].

$MoSe_2$ has attracted lots of interest due to its layered lattice structure and its band gap energy is well matched with the visible portion of the emission spectrum of the sun (1-2 eV) [18]. The direct band gap of $MoSe_2$ is 1.5 eV which is close to the optimum bandgap value of single-junction solar cells and photoelechemical devices. Similar to other TMDCs, $MoSe_2$ has potential applications as a photodetector, transistor, and chemical sensor [19].

WS_2 is a member of the TMDCs family [20] and is electronically similar to MoS_2 [21]. WS_2 has potential use in low cost photovoltaic cells, solid lubricants, and as a catalyst [22]. Monolayer WS_2 has the highest photoluminescence yield of all TMDCs studied to date with a very narrow spectral width [23].

1.2 Previous Studies of Elastic Properties of Transition Metal Dichalcogenides

As mentioned previously, $MoSe_2$, MoS_2 and WS_2 have attracted ongoing interest due to their remarkable optical, structural, and electronic properties. These properties have been increasingly subject to theoretical and experimental investigations [14, 24, 25]. Theoretical studies of the elastic properties of TMDCs have also received attention [26, 27]. However, only a few experimental studies of the elastic properties of these materials have been reported in the literature [28, 29]. Since this thesis is mainly concerned with the elastic properties of TMDCs, the following sections discuss some of the theoretical and experimental investigations of these properties.

1.2.1 Theoretical Studies

There have been several theoretical methods used for the determination of the elastic properties of TMDC [27, 30, 31]. Density functional theory (DFT) and first-principles calculations are examples of the most common theoretical approaches used in such determination. Duerloo *et al.* [26] calculated the band gaps, elastic constants, and piezoelectric coefficients of monolayer of $MoSe_2$, MoS_2 and WS_2 using DFT at the generalized gradient approximation level of theory. Li *et al.* [32], studied the effcet of pressure on the electronic structure and elastic properties of MoS_2 using first prin-

ciples calculations. They found that the band gap energy decreases as the pressure increases. They also mentioned that the elastic constants, C_{ij}, increase when the pressure increases.

Tunghathaithip *et al.* [30] used DFT to calculate the lattice constant, energy gap, and the elastic constants of $MoSe_2$, MoS_2 and WS_2. In particular, they calculated the elastic constants C_{11} and C_{12} of the aforementioned materials and found that their DFT-calculated elastic constants were in good agreement with those reported by Duerloo *et al.* [26] calculated with ab-initio approach. Peelaers *et al.* [33] measured the bulk elastic constants of MoS_2 theoretically by Hybrid-DFT. They compared their elastic constants with those obtained from neutron scattering experiments. The authors claimed that there was good agreement between C_{11}, C_{33} and C_{44} from these two methods, while some discrepancies were observed for C_{22}. Zeng *et al.* [34] also measured the band structure and elastic constants (*i.e*, C_{11}, C_{12} and C_{44}) in both monolayer and bilayer structures of $MoSe_2$, MoS_2 and WS_2 by first-principles study. They found that WX_2 compounds, (X = O, S, Se, Te) have greater elastic constants values than those of MoX_2 compounds.

Çakır *et al.* [27] performed first principles-based quasi-harmonic approximation calculations to characterize the mechanical and thermal properties of MX_2 monolayers, where X = O, S, Se, Te. Similar to the results obtained by Peelaers *et al.* [33], the elastic constants C_{11} and C_{12} were found to decrease as the number of chalcogenide layers increases. They also found that in each chalcogenide group, the metal became stiffer as the row number in the Periodic Table of the metal atom increases. The authors also suggested that the desirable mechanical and thermal proprieties of TMDCs materials indicate the potential of using such materials in nanoelectronic applications.

The elastic properties of 2H-and 3R-WS_2 were investigated with first-principles calculations while the pressure varied from 0 to 20 GPa by Feng *et al.* [35]. They found

that both 2H- and 3R-WS_2 at 0 GPa have large elastic anisotropy perpendicular and parallel to the layers. Also, they found that the elastic anisotropies in compressibility and shear became weak for both structures with increasing pressure. The elastic properties of 2H-MoS_2 was studied theoretically by [36]. They used periodic a Hartree-Fock method to measure the lattice constants and C_{11}, C_{33}, C_{12}, C_{13}, and C_{44}. Ref [37] also used Hartree-Fock and DFT methods to calculate the same parameters, the lattice constants and C_{11}, C_{33}, C_{12}, C_{13}, and C_{44} of 2H-MoS_2.

Acoustic phonons in TMDCs have also been studied theoretically. For example, Gu *et al.* [1] used the first-principles-driven phonon Boltzmann transport equation approach to calculate the lattice constants and the sound velocities of the three lowest phonon branches (longitudinal acoustic (LA), transverse acoustic (TA) and flexural acoustic (ZA)) of single layer TMDCs including $MoSe_2$, MoS_2, and WS_2. Kaasbjerg *et al.* [4] used first principles studies and measured phonon-limited mobility, electron-phonon interactions, deformation potentials, transverse (TA) and longitudinal (LA) sound velocities of single-layer MoS_2 above 100 K. Jin *et al.* [2] calculated drift velocities of MX_2 (M = Mo, W; X = S, Se) by a first-principles calculation of carrier-phonon interaction combined with the full-band Boltzmann equation. The electronic band structure and three acoustic and six optical modes of single layer $MoSe_2$ were obtained theoretically by Horzum *et al.* [3]. Phonon group velocities of $MoSe_2$, MoS_2, and WS_2 were calculated by Muratore *et al.* [38]. They studied the effect of domain size on phonon scattering, thermal conductivity, and group velocity of the mentioned materials. The acoustic velocities of $MoSe_2$, MoS_2, and WS_2 were also measured by full-potential local-orbital code [39].

1.2.2 Experimental Studies

As stated previously, there have been only a few experimental studies of the elastic properties of TMDCs. One of the experimental techniques for the measurement of the in-plane stiffness and breaking strength of a suspended monolayer and bilayer of MoS_2 is nanoindentation using an atomic force microscope (AFM). In the study reported by Bertolazzi *et al.* [40] it was found that a monolayer MoS_2 has exceptional mechanical properties comparable to stainless steel. In-plane stiffness of monolayer and bilayer of MoS_2 were measured and found to be 180 ± 60 Nm^{-1} and 270 ± 70 Nm^{-1}, respectively, while the Young's modulus was 270 ± 100 GPa, close to the Young's modulus of MoS_2 nanotubes (230 GPa), bulk MoS_2 (238 GPa), and steel (210 GPa). Feldman [41] used neutron scattering and X-ray measurements of the linear compressibilities of 2H-MoS_2 and 2H-$NbSe_2$ to obtain the elastic constants of these materials. They compared their results with results from model predictions of C_{33} and C_{44} and found good agreement between theoretical and experimental data.

Skolnick *et al.* [28] reported ultrasonic measurements of the transverse and longitudinal velocities of sound in 2H-$NbSe_2$ and TaS_2 at temperatures varying from 4 K to 220 K. Bhatt *et al.* [42] demonstrated the use of Raman spectroscopy to investigate the anharmonic nature of phonons in TMDCs and found that these materials do not undergo phase transitions at high-pressure and low-temperature range.

Brillouin scattering has also been used in the investigation of the elastic properties of TMDCs materials. This technique was used by Karanikas and Sooryakumar [43] to measure the elastic constants of hafnium disulfide (HfS_2). The six independent elastic constants C_{11}, C_{12}, C_{13}, C_{14}, C_{33} and C_{44} were extracted from bulk phonon velocities. Harley and Fleury [44] conducted Brillouin scattering studies to investigate the velocities of surface and bulk acoustic waves in 2H-$NbSe_2$ and TaS_2. Brillouin spectroscopy was also used by Akintola *et al.* [29] to study acoustic phonons in WSe_2.

The authors were able to obtain a Rayleigh surface phonon velocity for WSe_2 of 1340 $\pm$ 20 m/s.

1.3 Motivation

In this work the elastic properties of $MoSe_2$, MoS_2, and WS_2 are, for this first time, experimentally investigated using Brillouin light scattering. The main focus of this work is the determination of the acoustic phonon velocities in $MoSe_2$, MoS_2, and WS_2 at room temperature which subsequently allows for the estimation of one elastic constant. This work has been motivated by the fact that TMDCs materials, specifically $MoSe_2$, MoS_2, and WS_2, have outstanding physical properties, making such materials to be widely considered in practical applications [45]. For example, Pu *et al.* [46] demonstrated the use of atomically thin MoS_2 in transistor applications which is owing to its outstanding mechanical properties such as flexibility and stretchability. Wang *et al.* [47] also discussed the possibility of using TMDCs materials in energy conversion and storage fields. The applicability of these materials was also extended to include sensors, catalysis and Li-ion batteries [48, 49]. In order for these materials to successfully compete with existing technologies, a deeper understanding of their properties is necessary. In particular, knowledge of the elastic properties, from which other mechanical properties such as Young's modulus and compressibility can be determined, is essential for the integration of TMDCs materials into electronic and optomechanical device applications [50]. The results obtained in this work could also be compared with the results obtained from other theoretical and experimental studies of elastic properties of TMDCs. This comparison would be very helpful to investigate the reliability and accuracy of theoretical models and other experimental approaches for determination of elastic properties of TMDCs.

1.4 Scope

As mentioned, this thesis is mainly concerned with employing the Brillouin light scattering technique to investigate surface and bulk acoustic phonons in $MoSe_2$, MoS_2, and WS_2. Chapter 2 provides an introduction to elasticity theory and the theory of Brillouin light scattering. In Chapter 3, the experimental techniques and sample preparation are discussed in detail. Chapter 4 presents the results of the Brillouin light scattering experiments on $MoSe_2$, MoS_2, and WS_2. A detailed discussion of these results is also given in this chapter. Finally, a summary of the work presented herein and concluding remarks about the findings of this work are provided in Chapter 5.

Chapter 2

Theory

2.1 Elasticity Theory

It is a well-established fact that solid materials undergo a change in volume or shape (i.e. deformation) under the influence of applied force. This deformation alters the state of equilibrium in which material molecules or atoms are arranged before deformation. From a mathematical point view, this alteration results in the displacement of a point $\vec{r}$ in a solid from its equilibrium position to a new position. The equilibrium and deformed state of a point in a solid body can be defined by the displacement vector $\vec{u}$ [51]:

$$u_i = R_i - r_i \qquad (i = x, y, z) \tag{2.1}$$

where $\vec{R}$ is a vector defining the new position of the deformed point and $\vec{r}$ is the equilibrium position vector. For a given point in the medium where $\vec{r}$ is known, determination of the displacement of this point is possible when the vector $\vec{u}$ is given. In the case where a body experiences a rigid motion in which the relative displacement of points in the solid is not observed, no strain would develop in the solid. This indicates that the body was not deformed and thus it will not exhibit its elasticity [52].

The physical property termed elasticity is a description of the material's response to an applied force. Accordingly, materials are generally categorized into elastic and inelastic materials. The former term refers to a material that returns to its original shape and volume after the applied force has been removed. The latter type describes materials which experience a change in shape even after the removal of the external force.

The fundamental mathematical formula that relates the stress and strain of a deformed material was established by Hooke and is written as:

$$\sigma_{ij} = C_{ijkl}\epsilon_{kl} \tag{2.2}$$

where σ_{ij} and ϵ_{kl}, respectively, represent the second rank stress and strain tensors, C_{ijkl} is the fourth rank elasticity tensor whose components are the elastic constants. Because both stress and strain are symmetric tensors ($\sigma_{ij} = \sigma_{ji}$ and ϵ_{kl}=ϵ_{lk}) their matrix components (3×3) can be reduced to a six element column matrix (6×1). Symmetry considerations can also reduce the number of the elastic constants in the elastic tensor from 81 into 36, allowing Hooke's law to be written in a reduced matrix form as follows

$$\begin{bmatrix} \sigma_1 \\ \sigma_2 \\ \sigma_3 \\ \sigma_4 \\ \sigma_5 \\ \sigma_6 \end{bmatrix} = \begin{bmatrix} C_{11} & C_{12} & C_{13} & C_{14} & C_{15} & C_{16} \\ C_{12} & C_{22} & C_{23} & C_{24} & C_{25} & C_{26} \\ C_{13} & C_{23} & C_{33} & C_{34} & C_{35} & C_{36} \\ C_{14} & C_{24} & C_{34} & C_{44} & C_{45} & C_{46} \\ C_{15} & C_{25} & C_{35} & C_{45} & C_{55} & C_{56} \\ C_{16} & C_{26} & C_{36} & C_{46} & C_{56} & C_{66} \end{bmatrix} \begin{bmatrix} \epsilon_1 \\ \epsilon_2 \\ \epsilon_3 \\ \epsilon_4 \\ \epsilon_5 \\ \epsilon_6 \end{bmatrix} \tag{2.3}$$

where the Voigt notation (11→1, 22→2, 33→ 3, 23=32→4, 31=13→5, 12=21→6)

has been used.

The number of elastic constants characterizing a material depends on its crystal structure. Cubic crystals, for example, have three elastic constants (e.g. C_{11}, C_{12}, C_{44}) whereas hexagonal-structured materials are described by six elastic constants (C_{11}, C_{12}, C_{13}, C_{33}, C_{44}, and C_{66}) . Of these constants, five elastic constants are independent since C_{66}= $\frac{1}{2}$(C_{11}-C_{12}). For the materials used during the course of this thesis, which are a family of transition-metal dichalcogenide materials, their hexagonal structure make the number of the independent elastic constants five as mentioned above. In this case, the elastic constants tensor takes the form [52]:

$$C = \begin{bmatrix} C_{11} & C_{12} & C_{13} & 0 & 0 & 0 \\ C_{12} & C_{11} & C_{13} & 0 & 0 & 0 \\ C_{13} & C_{13} & C_{33} & 0 & 0 & 0 \\ 0 & 0 & 0 & C_{44} & 0 & 0 \\ 0 & 0 & 0 & 0 & C_{44} & 0 \\ 0 & 0 & 0 & 0 & 0 & C_{66} \end{bmatrix} \tag{2.4}$$

In Brillouin scattering, the long wavelengths of surface and bulk acoustic waves compared to the dimensions of the primitive cell make it possible to consider these waves as sound waves in a continuous medium [51]. As a result, the equation of motion for these waves can be expressed as:

$$\rho(\frac{d^2u_i}{dt^2}) = C_{ijkl}(\frac{d^2u_i}{dx_j dx_k}) \tag{2.5}$$

where ρ is the material density and u_i is the ith component of the displacement vector.

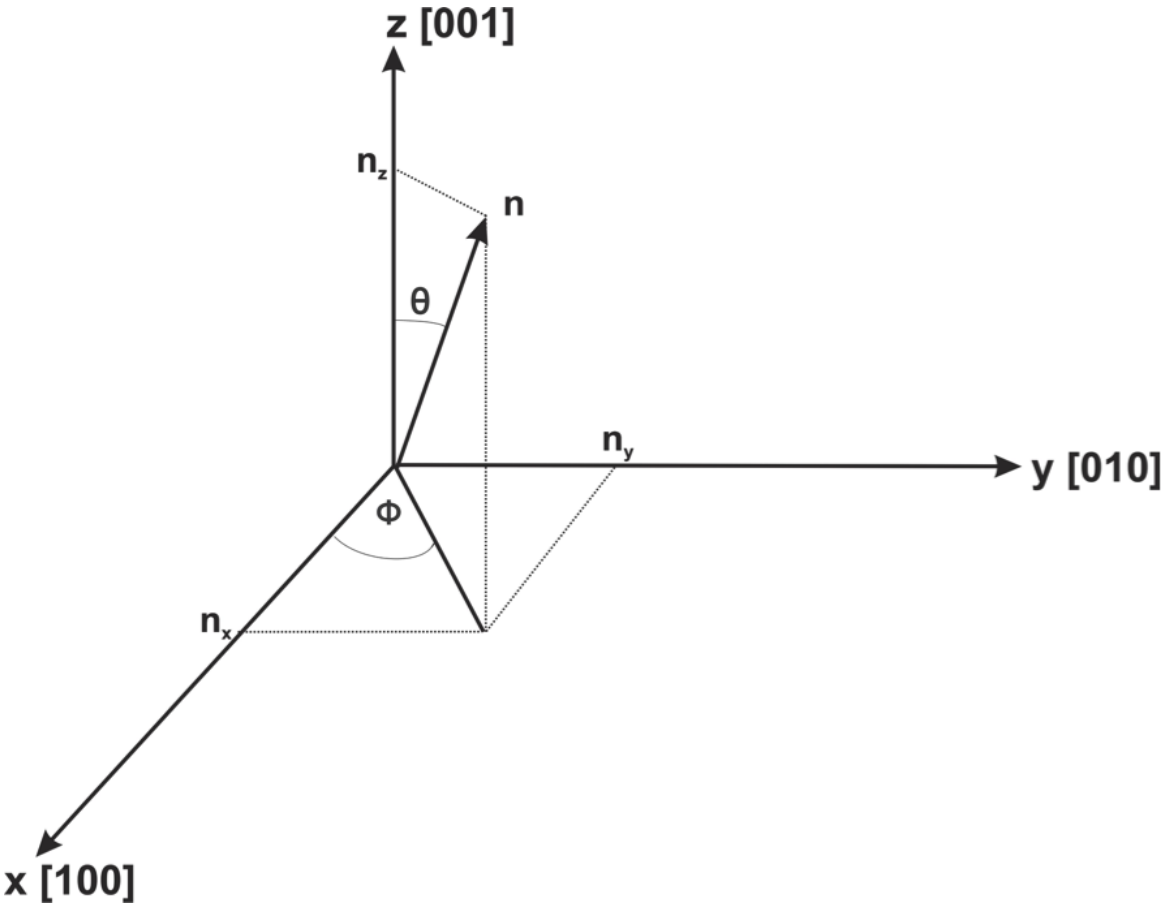

Figure 2.1: Direction cosines of $\widehat{n}$.

For plane waves, this displacement vector is given by:

$$\vec{u_i} = u_i e^{i(\vec{k}\cdot\vec{r}-wt)} \tag{2.6}$$

By substituting equation (2.6) into equation (2.5), the Christoffel equation from which the phase velocities of all possible wave modes can be computed is obtained as follows:

$$\rho v^2 \delta_{ij} - C_{ijkl} n_j n_k = 0 \tag{2.7}$$

where ρ is the material density, v is the phonon velocity, δ_{ij} is the Kronecker delta, and

$\widehat{n}$ is a unit vector that points in the direction of propagation. The elastic constants of a crystal are related to the propagation velocities of the acoustic waves and can be evaluated by solving the following equation :

$$\det \mid \Gamma_{ij} - \rho v^2 \delta_{ij} \mid = 0 \tag{2.8}$$

where $\Gamma_{ij} = C_{ijkl}\ n_j\ n_k$. This equation results in three real and positive eigenvalues ρv^2 for three different modes (i.e. two quasi-transverse and one quasi-longitudinal). For a phonon propagating in an arbitrary direction $\vec{n}$ in a hexagonal anisotropic solid, the Christoffel equation (2.8) can be expressed as :

$$\begin{bmatrix} C_{11}n_x^2+C_{66}n_y^2+C_{44}n_3^2-\rho v^2 & (C_{12}+C_{66})n_x n_y & (C_{13}+C_{44})n_x n_z \\ (C_{12}+C_{66})n_x n_y & C_{11}n_x^2+C_{66}n_y^2+C_{44}n_3^2-\rho v^2 & (C_{13}+C_{44})n_y n_z \\ (C_{13}+C_{44})n_x n_z & (C_{13}+C_{44})n_y n_z & C_{44}n_x^2+C_{44}n_y^2+C_{33}n_3^2-\rho v^2 \end{bmatrix} = 0 \tag{2.9}$$

For propagation along z direction [001], where $\mathrm{n}_x = \mathrm{n}_y = 0$, the Christoffel equation is expressed as [53]:

$$\begin{bmatrix} C_{44}n_z^2 - \rho v^2 & 0 & 0 \\ 0 & C_{44}n_z^2 - \rho v^2 & 0 \\ 0 & 0 & C_{33}n_z^2 - \rho v^2 \end{bmatrix} = 0. \tag{2.10}$$

From Equation (2.10), it can be realized that there are only two elastic constants C_{33} and C_{44}. Along this direction, the first and second plane waves are transverse polarized along x =[100] and y =[010] having the same velocity which is given by

$$v_T = \sqrt{\frac{C_{44}}{\rho}}. \tag{2.11}$$

The third wave is a longitudinal wave polarized along z =[001] with a velocity

$$v_L = \sqrt{\frac{C_{33}}{\rho}}. \tag{2.12}$$

2.2 Light Scattering

Brillouin light scattering (BLS) is the inelastic scattering of monochromatic laser light by acoustic phonons in the GHz frequency range [54]. The main use of Brillouin scattering is to determine acoustic phonon velocities and elastic properties of materials [55]. The scattering event can be described in terms of energy and momentum conservation laws. The conservation equations may be written as:

$$\hbar\omega_i \pm \hbar\omega = \hbar\omega_s \tag{2.13}$$

$$\hbar\vec{k}_i \pm \hbar\vec{k} = \hbar\vec{k}_s \tag{2.14}$$

where ω_i, ω_s, and ω are the angular frequencies of the incident and scattered photons and acoustic phonons, respectively. $\vec{k}_i$, $\vec{k}_s$, and $\vec{k}$ are the wavevectors of incident and scattered photons and acoustic phonons, respectively. From an energy point of view, one can notice that the scattered light changes its angular frequency from ω_i to ω_s by an inelastic interaction, in which a photon can be either created, known as Stokes process, or annihilated, known as anti-Stokes process. In Stokes scattering, (subtraction in equations (2.13) and (2.14)) the photon creates a phonon by transferring the momentum to atoms of the sample, therfore it loses momemtum and energy. In anti-Stokes scattering, (addition in equations (2.13) and (2.14)) the photon annihilates an existing phonon, hence its energy and momentum increase [56]. These processes are shown in Figure (2.2).

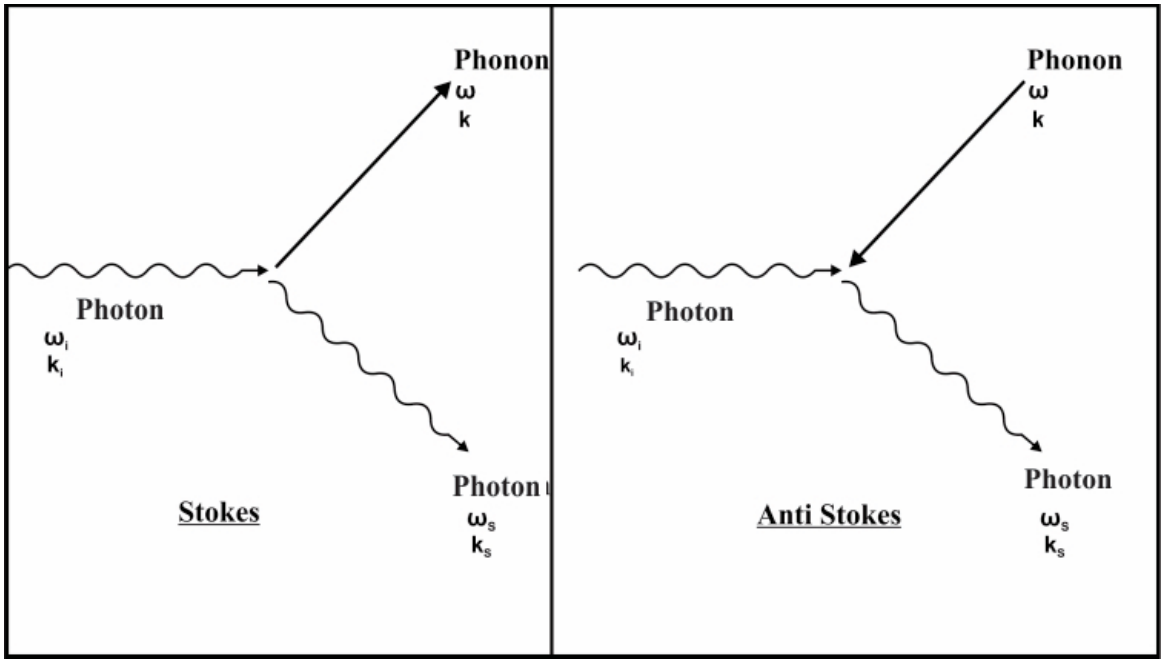

Figure 2.2: Schematic of the Stokes scattering (creation) and anti-Stokes scattering (annihilation).

In a solid there are two different mechanisms by which the photon can be scattered by acoustic waves, namely the bulk elasto-optic and the surface ripple mechanisms. The former occurs in the bulk, while the later occurs at the surface. In the elasto-optic mechanism, the coupling between the incident and scattered light occurs due to the acoustic modulation of the dielectric constant of the sample [57]. In the surface ripple effect, due to the dynamic acoustic deformation of the surface, only the wavevector component that is parallel to the surface is conserved; and the light is scattered from the surface. There are two types of acoustic modes named as bulk and surface modes, detectable by Brillouin scattering [58]. In opaque materials, due to an increase in the imaginary part of the refractive index (extinction coefficient), the contribution from surface ripple effect dominates over the contribution from elasto-optic mechanism.

In general, the spectrum of the scattered light has information on both bulk and surface acoustic phonons. In this work, experiments were conducted in 180° backscat-

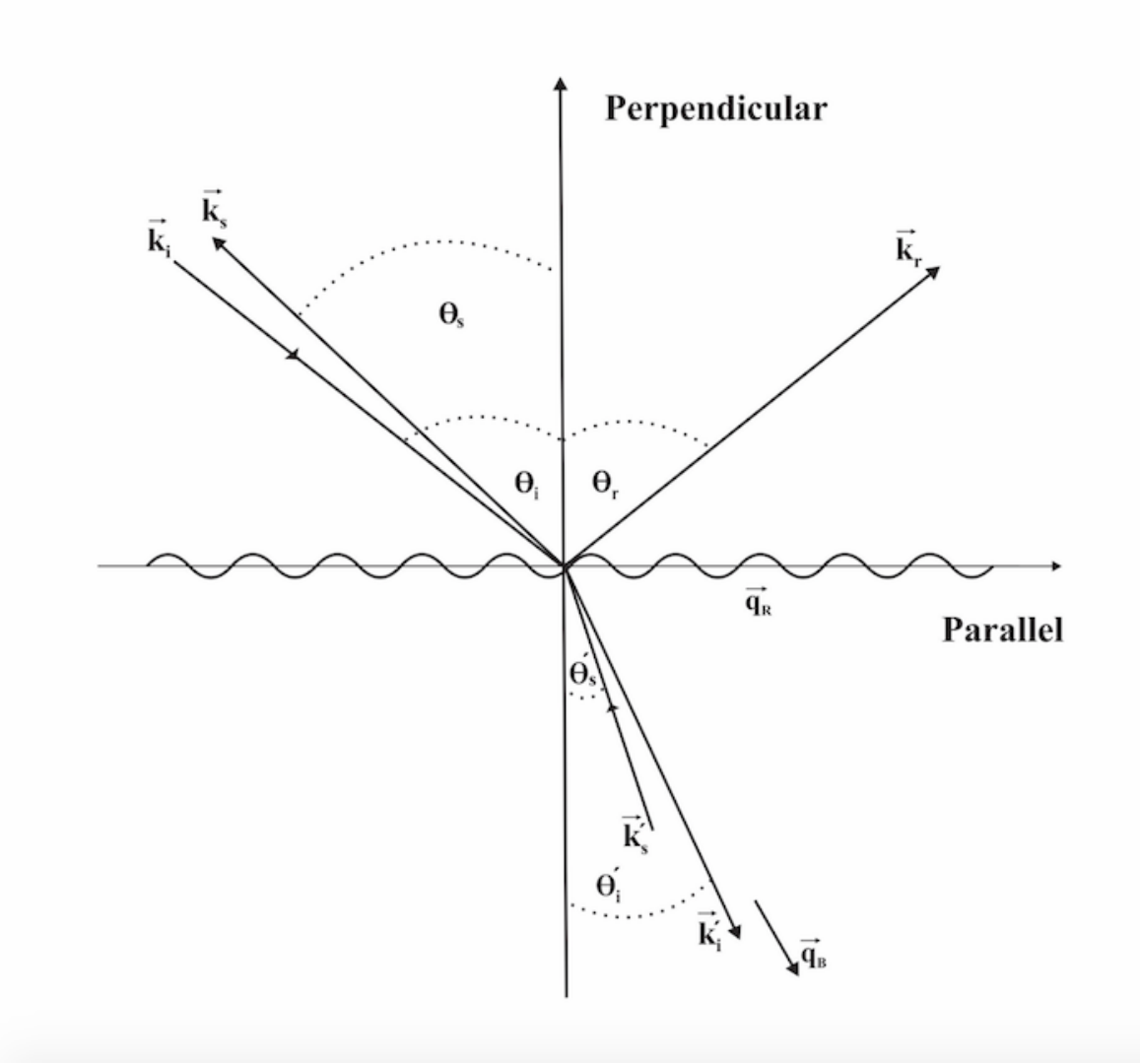

Figure 2.3: Schematic of Brillouin scattering geometry, where $\vec{k}_r$, $\vec{k}_i$, and $\vec{k}_s$ are the reflected, the incident and scattered photon wave vectors, θ_i and θ_s are the angles that the wave vectors of the incident and scattered light make with the surface normal. $\vec{q}_B$ and $\vec{q}_R$ are bulk and surface phonon wave vectors. In backscattering geometry $\theta_i \simeq \theta_s$.

tering geometry. This geometry is shown in Figure (2.3).

2.2.1 Scattering from Bulk Modes

As can be seen in Figure (2.4), the magnitude of the bulk phonon wavevector $\vec{q}_B$ can be calculated by the following equation

$$q_B^2 = (\frac{2\pi\nu}{v})^2 = k_i^2 + k_s^2 - 2\vec{k}_i \cdot \vec{k}_s \tag{2.15}$$

The phonon frequency, ν, is several orders of magnitude smaller than ν_i and ν_s. This means that $\nu_i \approx \nu_s$ and therefore $k_i \approx k_s$. Using the cosine rule equation (2.15) can be written as

$$q_B^2 = 2{k_i}^2(1 - \cos\theta) = 4k_i^2 \sin^2\frac{\theta}{2} \tag{2.16}$$

or

$$q_B = 2k_i \sin\frac{\theta}{2} \tag{2.17}$$

where θ is the scattering angle (here equal to 180°).

The angular frequency of a bulk phonon, ω_B, is given by

$$\omega_B = 2\pi f_B = v_B q_B, \tag{2.18}$$

where f_B is the phonon frequency and v_B is a bulk acoustic phonon velocity (either quasi-transverse or quasi-longitudinal). The magnitude of the incident light wavevector is given by $k_i = \frac{2n\pi}{\lambda_i}$ and using equation (2.18), the frequency of the bulk modes is written as

$$f_B = \frac{2nv_B}{\lambda_i}. \tag{2.19}$$

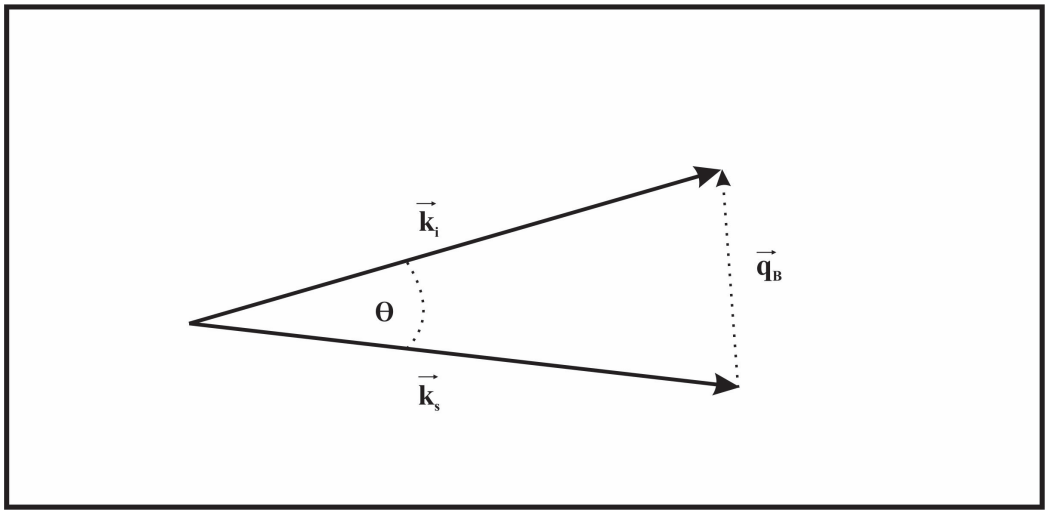

Figure 2.4: Relationship between incident light wave vector, $\vec{k}_i$, scattered light wave vector, $\vec{k}_s$, and phonon wavevector, $\vec{q}_B$.

2.2.2 Scattering from Rayleigh Surface Modes

In scattering from surface modes, the perpendicular component of wavevector conservation condition is not valid anymore. The reason for that is because the phonon amplitude decreases to zero at a short distance below the surface [59]. In this case one should replace equations (2.13) and (2.14), with

$$q_R = k_i \sin\theta_i + k_s \sin\theta_s = k_i(\sin\theta_i + \sin\theta_s) \tag{2.20}$$

where θ_i is the angle of the incidence and θ_s is the angle that the scattered light makes with the normal to the surface (see Figure 2.3), and k_i and k_s are the wavevectors of the incident and scattered light, respectively. Using the fact that in a 180° backscattering geometry, $\theta_i \simeq \theta_s$, equation (2.20) may be written as :

$$q_R = 2k_i \sin\theta_i. \tag{2.21}$$

Also, the angular frequency of the Rayleigh surface phonon, ω_R, is given by

$$\omega_R = 2\pi f_R = v_R q_R \tag{2.22}$$

where f_R is the phonon frequency and v_R is the surface acoustic phonon velocity. By substituting $k_i = \frac{2\pi}{\lambda_i}$ in equation (2.21), equation (2.22) can be written as

$$f_R = \frac{2v_R \sin\theta_i}{\lambda_i}. \tag{2.23}$$

Equation (2.23) gives the frequency of the Rayleigh surface phonon.

If incidenct light wavelength, λ_i, and the refractive index, n, are known then equations (2.19) and (2.23) can be used to determine acoustic mode velocities. Figure (2.5) shows a schematic representation of a typical Brillouin spectrum. The peaks due to the surface, or Rayleigh peaks, are labeled as R, where the frequency shift is dependent on the angle of incidence according to Eq. (2.23). Also, the peaks from the bulk, including two quasi-transverse and one quasi-longitudinal, are shown as QT and QL, respectively. All the peaks are located symmetrically on both sides of the central elastic peak, while the left and the right hand side peaks correspond to Stokes and anti-Stokes processes, respectively. The velocity of the quasi-transverse mode and the velocity of transverse mode are equal if they are travelling along z direction. Phonon probed in this work at small θ_i within 10° in direction close to z direction.

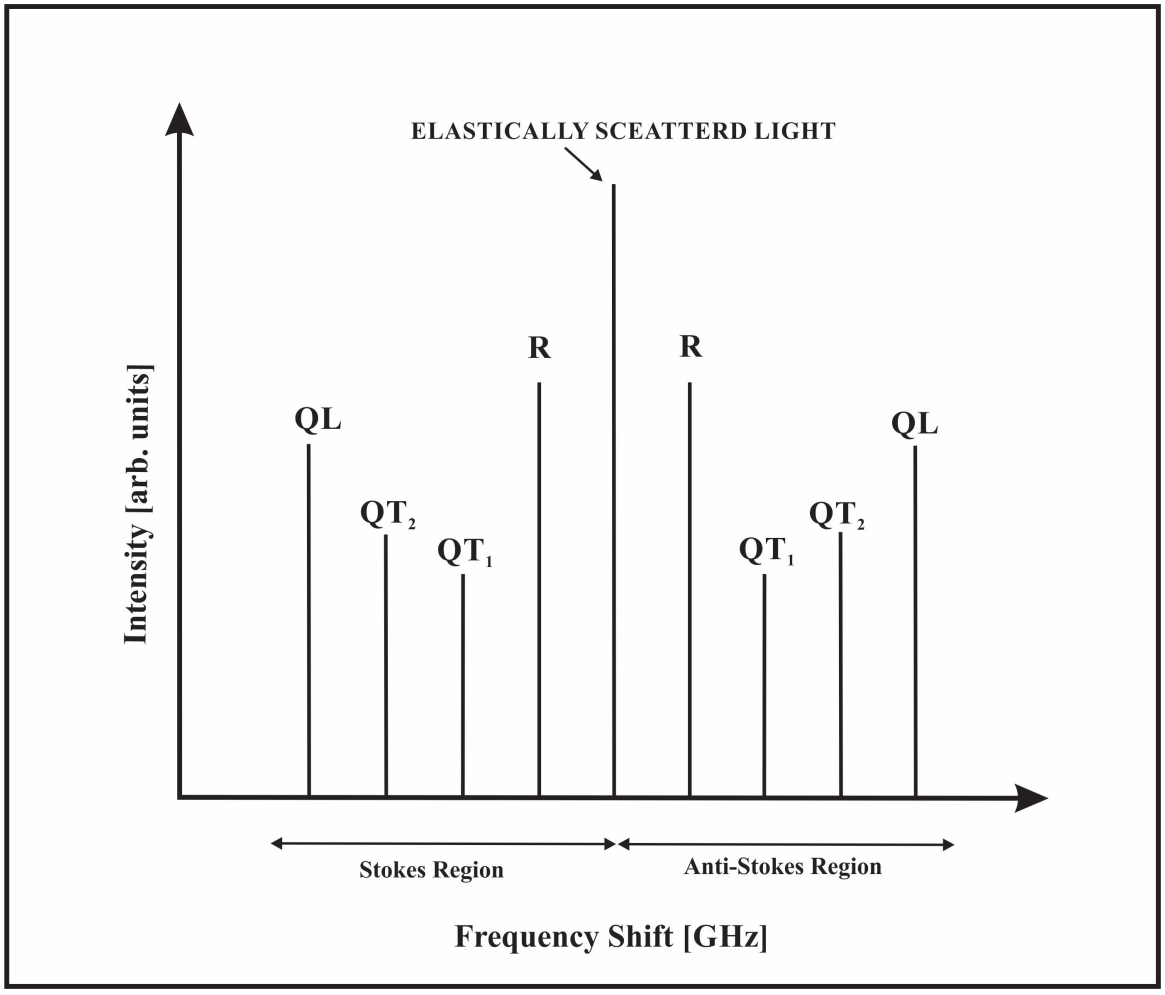

Figure 2.5: Schematic of a Brillouin spectrum. Peaks appear on both sides of the central peak, corresponding to Stokes and anti-Stokes scattering. R : Rayleigh surface mode peak, QT : quasi- transverse bulk mode peak,QL: quasi-longitudinal bulk mode peak.

Chapter 3

Experimental Details

3.1 Introduction

In this chapter the process used to synthesize the crystals of $MoSe_2$, MoS_2 and WS_2 is presented. A detailed desciption of the optical system used for the Brillouin light scattering experiments is also included.

3.2 Sample Fabrication

The samples of $MoSe_2$, MoS_2 and WS_2 used in this work were made by the Keppens research group at The University of Tennessee, Knoxville. In short, MX_2 polycrystalline compounds were first synthesized from stoichiometric mixtures of tungsten (99.999 %), molybdenum (99.999 %), selenium (99.999 %), and sulfur (99.9995 %) powders. Each mixture was sealed in a silica tube under vacuum. The mixture was then heated to 900°C over the span of 4-5 days. It was then kept at room temperature for 7 days to cool down.

A chemical vapor transport method was used to grow single crystals of the resulting polycrystalline compounds using a transport agent of iodine. Silica tubes containing

polycrystalline MX_2 powder and roughly 17.5 mg of iodine were sealed under vacuum and heated at a rate of 1° C/minute in a tube furnace to achieve a 50° C temperature gradient from the hotter end of the tube (950-1050°C) to the colder end where crystal growth occurs (900-1000°C). This temperature profile was maintained for 5-10 days, at which point the tube was allowed to cool down and the samples removed. In this work, two samples for each MoS2 and MoSe2 were used. There are no differences between the two samples of the same material.

The samples were thin flakes approximately hundred micrometers thick and about 5 millimeter in diameter. They were silvery black in colour. The surface plane is the basal plane of hexagonal crystal. Figure 3.1 shows photographs of the three material.

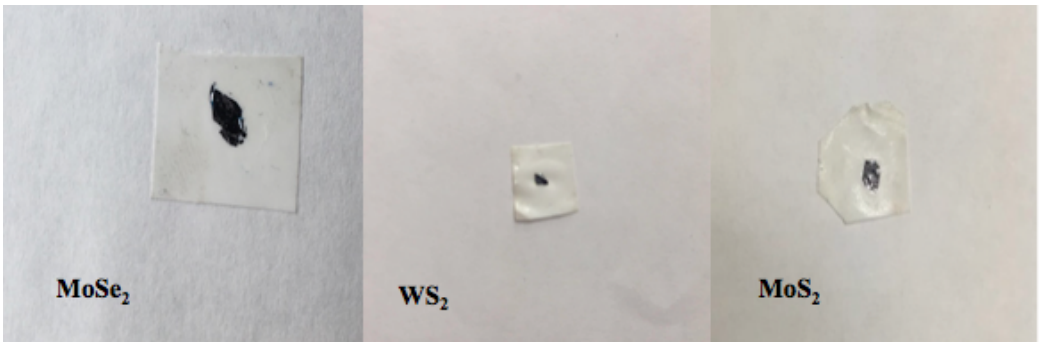

Figure 3.1: Photograph of $MoSe_2$, MoS_2 and WS_2 crystals used in this study.

3.3 Optical System

Figures 3.2 and 3.3 show a schematic diagram and a photograph of the optical setup used in this project, respectively. The light source was a Coherent Verdi-V2 diode pumped Nd:YVO_4 laser, operating on second harmonic with wavelength of 532 nm. The bandwidth of the laser beam is ∼10 MHz and it is vertically polarized. For the current work, the laser beam power was set to 60 mW. The laser beam first passes through a variable neutral density filter ($VNDF_1$). The VNDF filters prevent

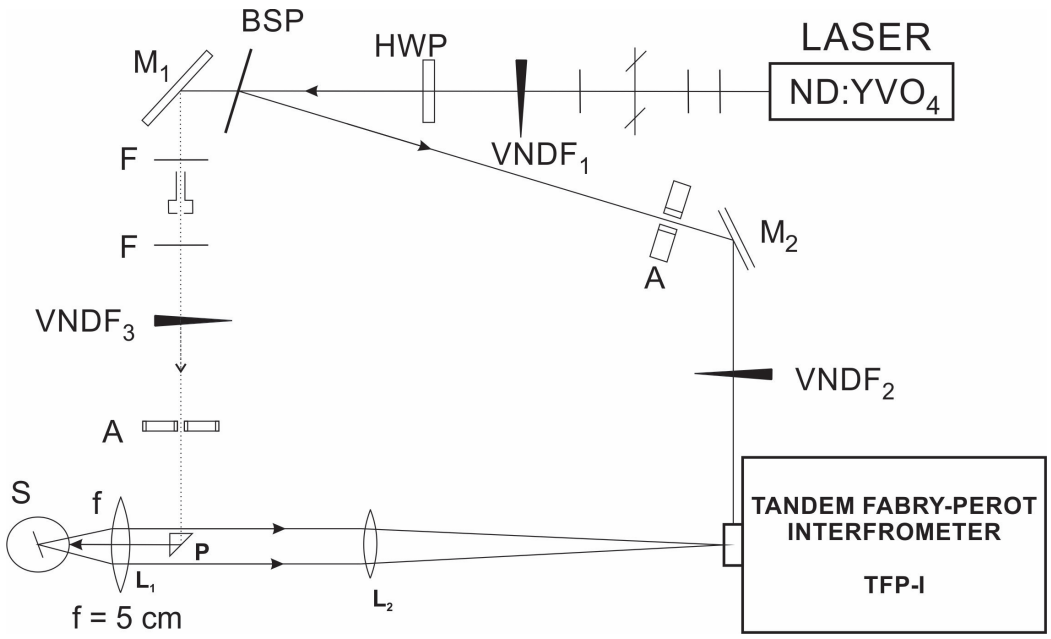

Figure 3.2: A: Schematic diagram of the experimental setup used for Brillouin light Scattering where N d: YVO_4 -laser, HWP-half wave plate, BSP- beam splitter, M-mirror, F-filter,VNDF- variable neutral density filter, A-aperture, L-lens,P-prism, f-foucsinglens, TFP-1-tandem Fabry-Perot interferometer.

damage to the sample by reducing the beam power. A half wave plate (HWP) was used to rotate the plane of polarization from vertical to horizontal. The horizontally polarized beam goes through a beam splitter (BSP) where a small fraction of its power is reflected to mirror M_2 and directed to the tandem Fabry-Perot interferometer TFP-1. This beam is used as reference beam in order to maintain the mirror alignment for both interferometers. Also, it is used to prevent the saturation of the photomultiplier tube by means of a shutter system. It occurs by providing a beam to the FPI while scanning over the region of the spectrum in which the elastic scattering happens nears 0 GHz frequency shift. The scattered light from the sample is very strong and it is blocked by a shutter on the FPI entrance pinhole.

The light transmitted through the beam splitter (BSP) hits mirror M_1 and is then directed through filters and $VNDF_3$ to the prism P. The beam then undergoes total internal reflection in the prism to change its direction by 90° and finally, the light is

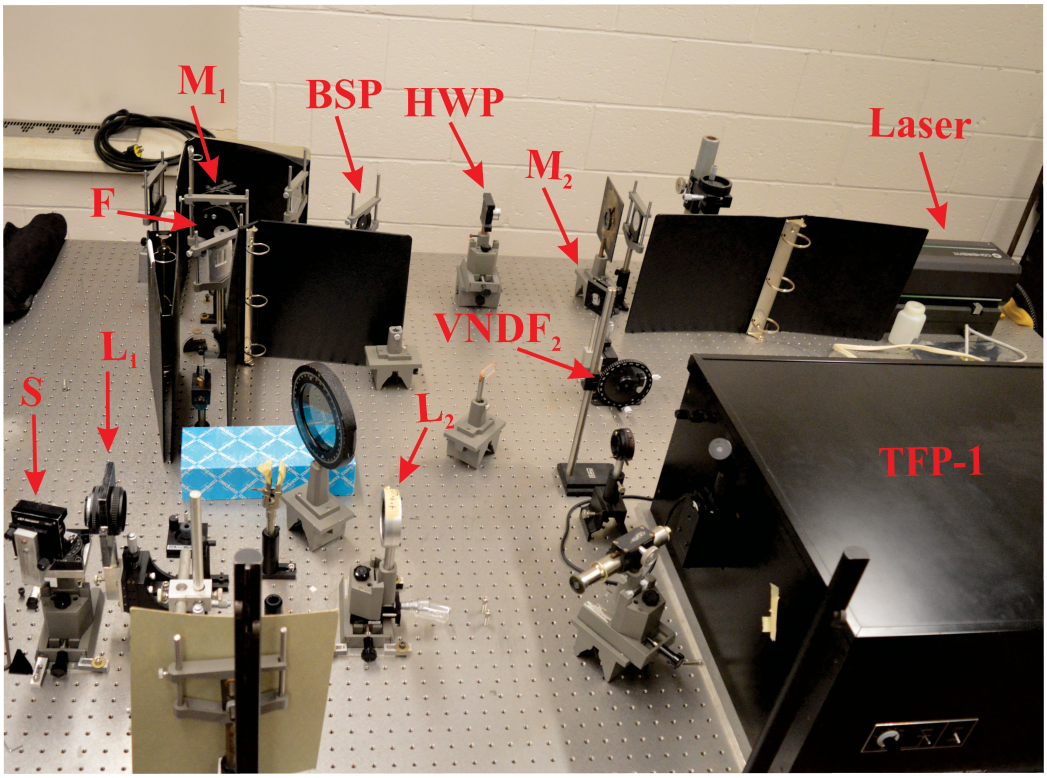

Figure 3.3: Photograph of Brillouin Scattering System.

focused on the sample S using lens L_1 with focal length of 5 cm. This lens also collects scattered light from the sample at 180° with respect to the incident light. The lens L_2, with focal length 40 cm, is used to focus the scattered light on the adjustable entrance pinhole of the Fabry-Perot interferometer. The pinhole size used in these experiments was 450 μm. The scatted light then enters the tandem Fabry-Perot interferometer TFP-1 to be frequency-analyzed.

In its basic form, a Fabry-Perot Interferometer is composed of two accurately parallel and plane mirrors, one of which is fixed while the other one is movable. These mirrors face each other and are separated by a distance L. The reflectivity of these two mirrors is normally very high (90%). The incident beam on a Fabry-Perot interferometer undergoes multiple internal reflections between the two mirrors. Constructive interference for normal incidence occurs when the following condition is

satisfied:

$$m\lambda = 2L \tag{3.1}$$

where m is an integer, and λ is the wavelength of the light inside the interferometer [54]. The resonance frequencies ν_m of an interferometer are given by [60]

$$\nu_m = m(c/2L) = m\nu_F \tag{3.2}$$

where c is the speed of light. ν_F is the difference between two successive resonant frequencies and is called free spectral range (FSR) (as shown in Figure 3.4). It is typically chosen to include the range of frequency where Brillouin peaks due to acoustic phonons appear. Brillouin shifts in this work are between 10 and 50 GHz and so the FSR was set to values from 15 GHz to 150 GHz.

Another important quantity related to Fabry-Perot interferometer is the finesse. The finesse is defined as the ratio of FSR to the full width at half maximum δF of the central elastic peak:

$$F = \frac{FSR}{\delta F}. \tag{3.3}$$

The finesse is dependent on the reflectivity and flatness of the Fabry-Perot mirrors. Finesse is not greater than 100 due to the limitations on the quality of the mirrors. The higher the finesse, the better the resolution of the Fabry-Perot interferometer.

The Fabry-Perot interferometer used in these studies is a Sandercock type, 6-pass tandem FPI (see Figure 3.5). In this instrument, two FPIs are operated in tandem to increase the contrast which allows very weak signals to be observed. An increase in the free spectral range at a fixed resolution [61] is also achieved using this configuration. The two interferometers in this system are the same but with a slight difference in mirror separation.

A slight change in spacing of both interferometers must fulfill the following equa-

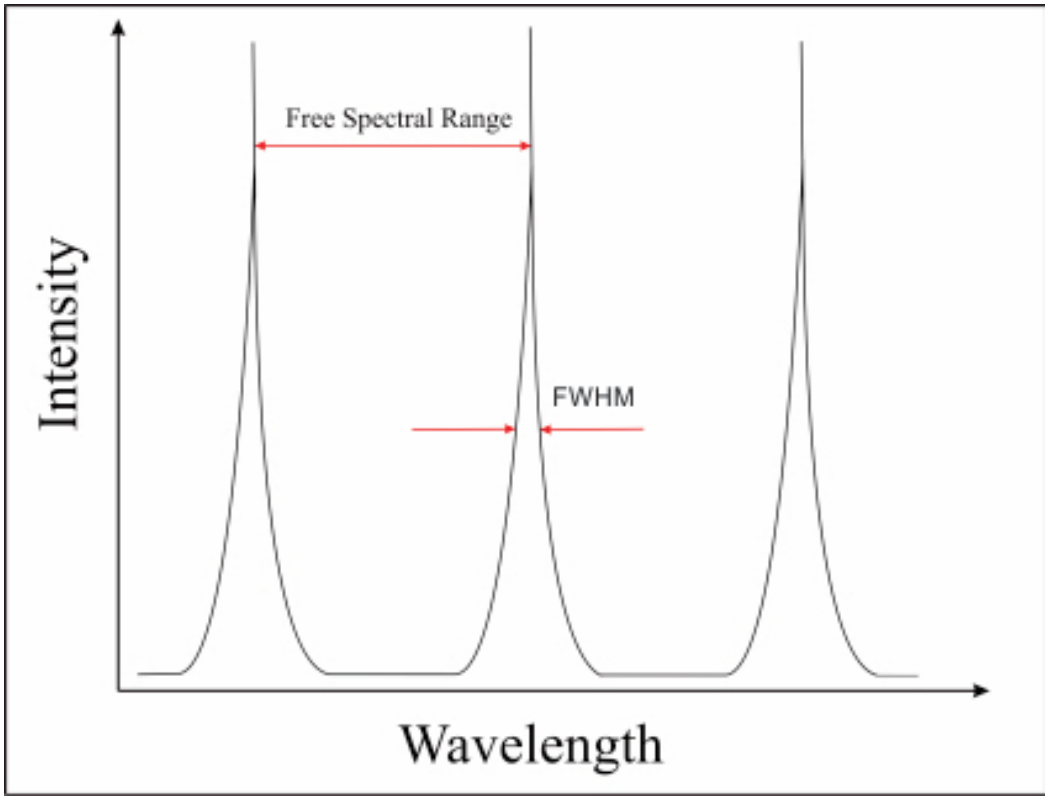

Figure 3.4: The spacing between two adjacent transmission maxima is the free spectral range FSR.

tion

$$\frac{\delta L_1}{\delta L_2} = \frac{L_1}{L_2} = \frac{1}{\cos\psi} \tag{3.4}$$

L_1 and L_2 are the distances between the mirrors in the first and the second interferometer, respectively, and ψ is the angle between them (as shown in Figure 3.5). In both interferometers, one mirror is fixed and the other one is movable. The movable mirrors are positioned on the same platform and are moved simultaneously.

Figure 3.6 shows the path of the light inside the Fabry-Perot interferometer enclosure. Upon entering the input aperture $A1$ the light is incident on the mirror M1. The reflected light from mirror M1 is collected by lens L_1 before hitting M2. The reflected beam from mirror M2 is incident on the first Fabry-Perot Interferometer, FPI1, and then passes through the aperture A2. The light passes through the second

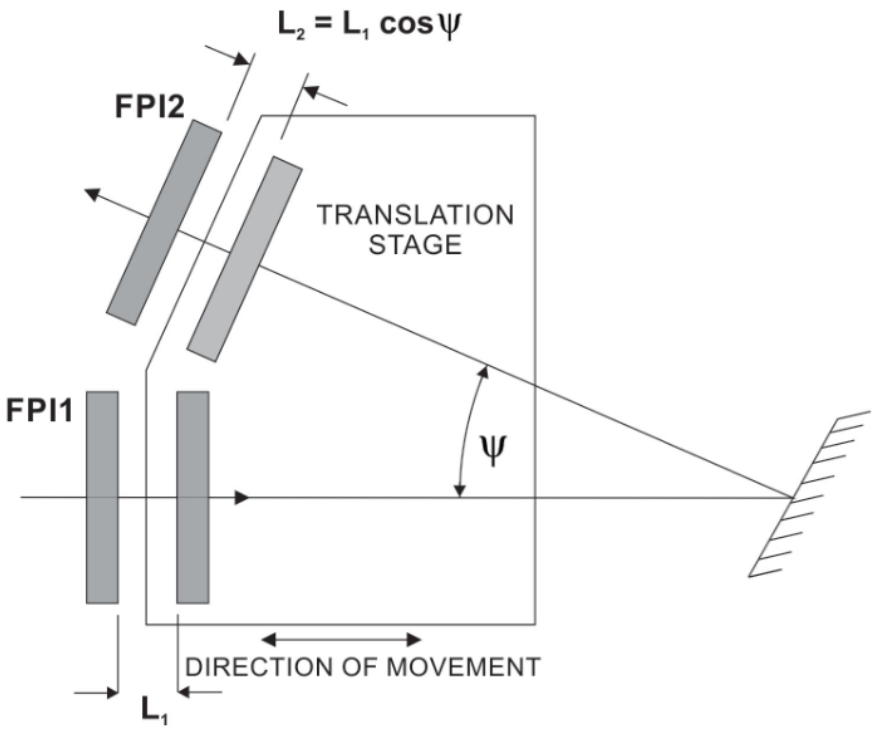

Figure 3.5: Schematic diagram of Tandem Fabry- Perot interferometer.

Fabry-Perot Interferometer, FPI2, after being reflected by mirror M3. The light hits the prism P1 and then reflected toward M4 parallel to the original direction. Mirror M4 reflects the light back for a third time through the system. This time the light hits mirror M5, the prism P2, mirror M6, aperture A3 and finally the adjustable output pinhole. The output pinhole size for this set of experiments was set to 700 μm. The light passes through the two FPIs three time before being transmitted to the photodetector. The stabilizing control maintains both parallel alignment of the mirrors as well as the spacing between them. This is carried out by control electronics. Control electronics applies voltage to piezoelectric crystals to tilt the mirrors in order to keep them parallel to one another. The FPI is isolated from extraneous vibration by a vibration isolation unit.

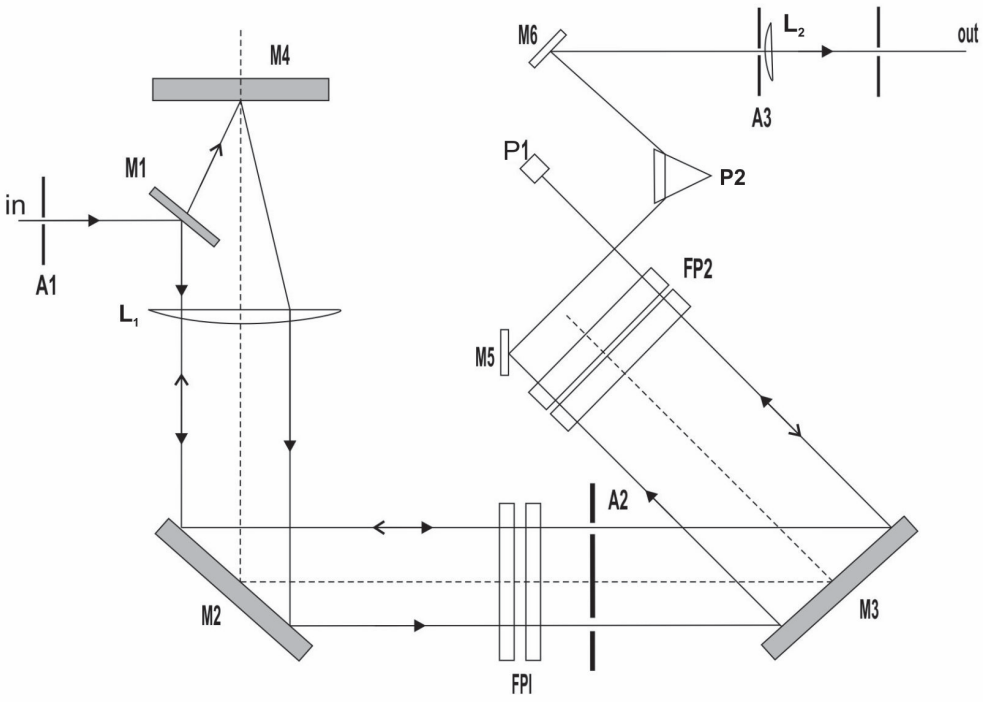

Figure 3.6: Schematic diagram of optic process inside the Fabry-Perot interferometers where FPI1 and FPI2 are Fabry-Perot interferometers,P1and P2 are prisms, M1, M2, M3, M4, M5, and M6 are mirrors, A- aperture, in-input pinhole, out-output pinhole.

Chapter 4

Results and Discussion

4.1 Introduction

In this chapter, the experimental results obtained with the Brillouin scattering technique for WS_2, $MoSe_2$ and MoS_2 are presented. These results of measured velocities and calculated elastic constants are subsequently discussed in detail and compared with theoretical and experimental data obtained with different techniques.

In this work, room temperature Brillouin scattering experiments were conducted on the TMDCs materials at different incidence angles varying from 15° to 75°. Each spectrum took almost twenty-six hours to collect. For MoS_2 and $MoSe_2$, two samples were investigated, while for WS_2 only one sample was available for study. Two different types of modes were observed by varying the free spectral range, namely the Rayleigh mode and transverse bulk modes. While the peak due to Rayleigh mode can be observed at lower free spectral range, the transverse bulk peaks can be found at higher frequency shifts. Rayleigh surface and transverse bulk acoustic phonon velocities were obtained from the Brillouin peak frequency shifts. Elastic constant C_{44} was also estimated for MoS_2 and WS_2 from the transverse acoustic phonon velocities and the

material densities.

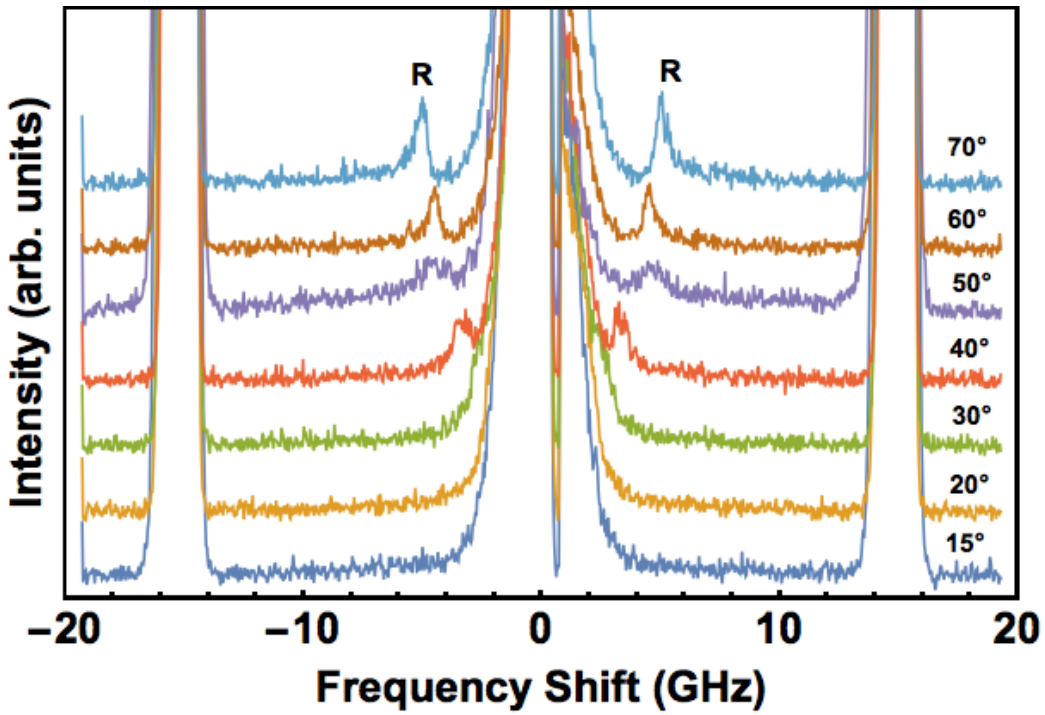

Figure 4.1: Brillouin spectra collected from WS_2. The free spectral range was set to 15 GHz. The numbers on the right hand side of the each spectrum indicate the incident angles.

4.2 Tungsten Disulphide WS_2

Figure (4.1) shows Brillouin spectra collected from the sample of WS_2 for angles of incidence ranging from 15° to 70°. The FSR was 15 GHz, corresponding to an interferometer mirror spacing of 7.50 mm. A single Brillouin doublet (labeled R) was observed for $\theta_i > 30°$. As can be seen, the frequency shift of this peak increases with increasing angle of incidence. The values of the average frequency shift are summarized in Table (4.1), and were measured by averaging the shifts of the Stokes and anti-Stokes peaks. The uncertainties are estimated based on the difference between the position of the peak and two channel displacement of the cursor which corresponds

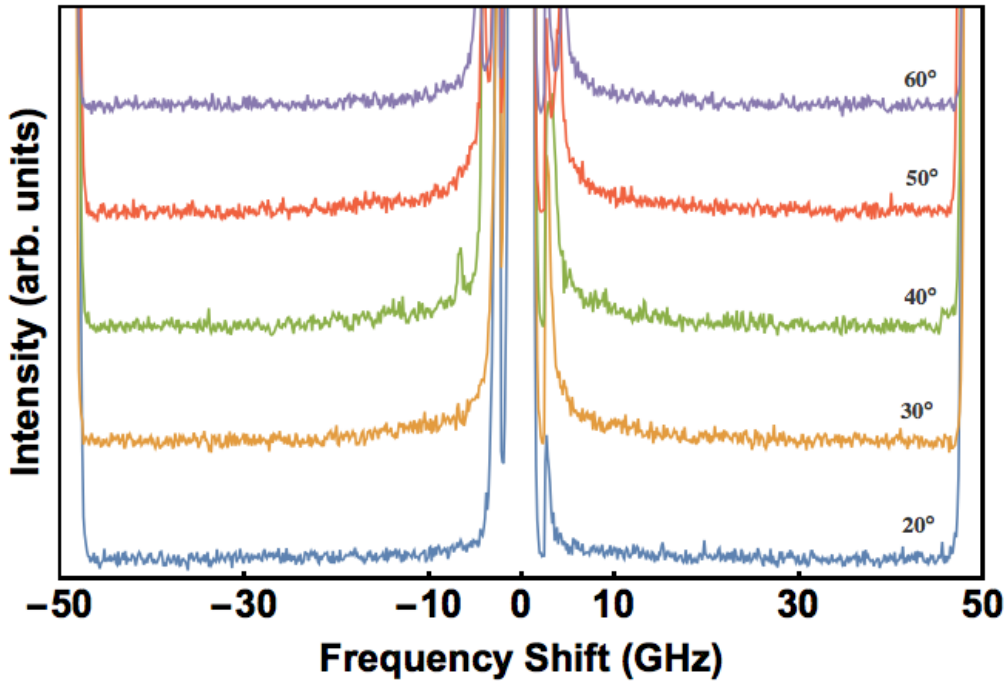

Figure 4.2: Brillouin spectra collected from WS_2. The free spectral range was set to 50 GHz. The numbers on the right hand side of the each spectrum indicate the incident angles.

to approximately 0.1 GHz.

In an effort to observe bulk mode peaks at higher frequency shifts, the FSR was increased to 50 GHz. No additional peaks were observed (see Figure 4.2). A further increase of the FSR to 150 GHz revealed weak broad peaks at frequency shifts of ∼44 GHz (see Figure 4.3). The shifts of these peaks have only a weak dependence on the angle of incidence and therefore cannot be due to surface modes. Due to the range of angles used here was 20° to 70°, the range of directions probed inside the material was found by Snell's law to be 3° to 9°. This allows these peaks to be classiffed as due to bulk modes. These spectra are also shown in Figure (4.4) in order to more clearly show the bulk modes (labelled T). The values of the average frequency shift are summarized in Table (4.1), and were measured by averaging the shifts of the Stokes and anti-Stokes peaks.

Table 4.1: Stokes (S), anti-Stokes (AS), and average (AVE) Brillouin frequency shifts for Rayleigh surface and transverse bulk modes of WS_2.

FSR	Material	Angle of Incidence (∘)	f_R^S (±0.1 GHz)	f_R^{AS} (±0.1 GHz)	f_R^{AVE} (±0.1 GHz)	f_T^S (±0.5 GHz)	f_T^{AS} (±0.5 GHz)	f_T^{AVE} (±0.5 GHz)
15	WS_2	70	5.0	5.0	5.0	-	-	-
		60	4.5	4.5	4.5	-	-	-
		50	4.4	4.6	4.5	-	-	-
		40	3.2	3.2	3.2	-	-	-
						-	-	-
150	WS_2	60	-	-	-	44.9	44.9	44.9
		50	-	-	-	44.9	44.9	44.9
		40	-	-	-	43.3	44.9	44.1
		30	-	-	-	43.9	44.0	43.9
		20	-	-	-	43.9	43.9	43.9

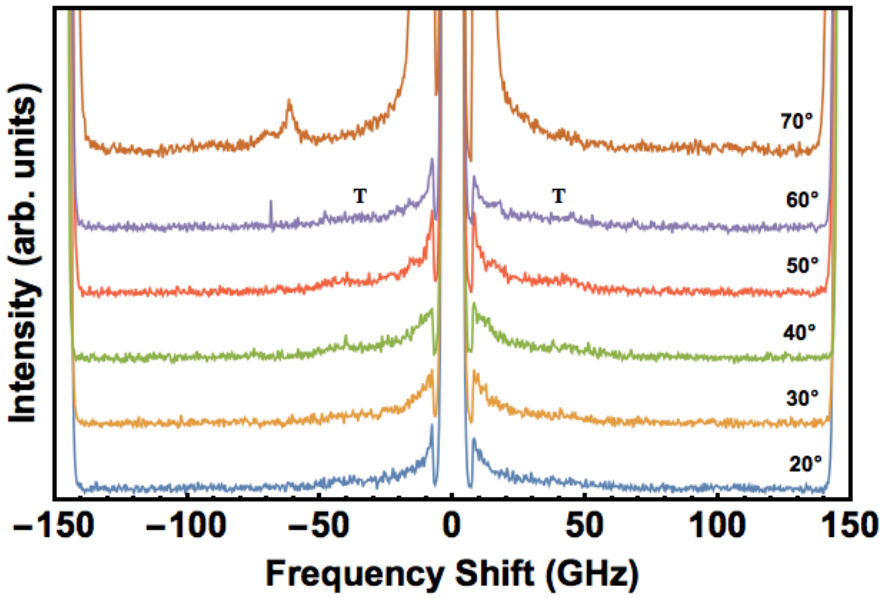

Figure 4.3: Brillouin spectra collected from WS_2. The free spectral range was set to 150 GHz. It is obseved that peaks attributed to bulk modes (T) can be noticed.

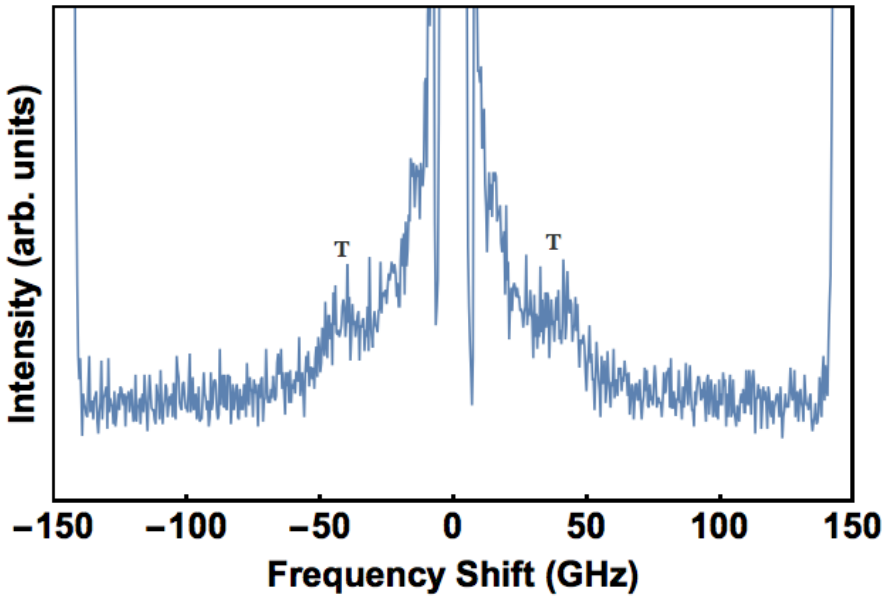

Figure 4.4: Individual spectrum collected from WS_2 at an angle of incident of 50° showing T peak. The free spectral range was set to 150 GHz.

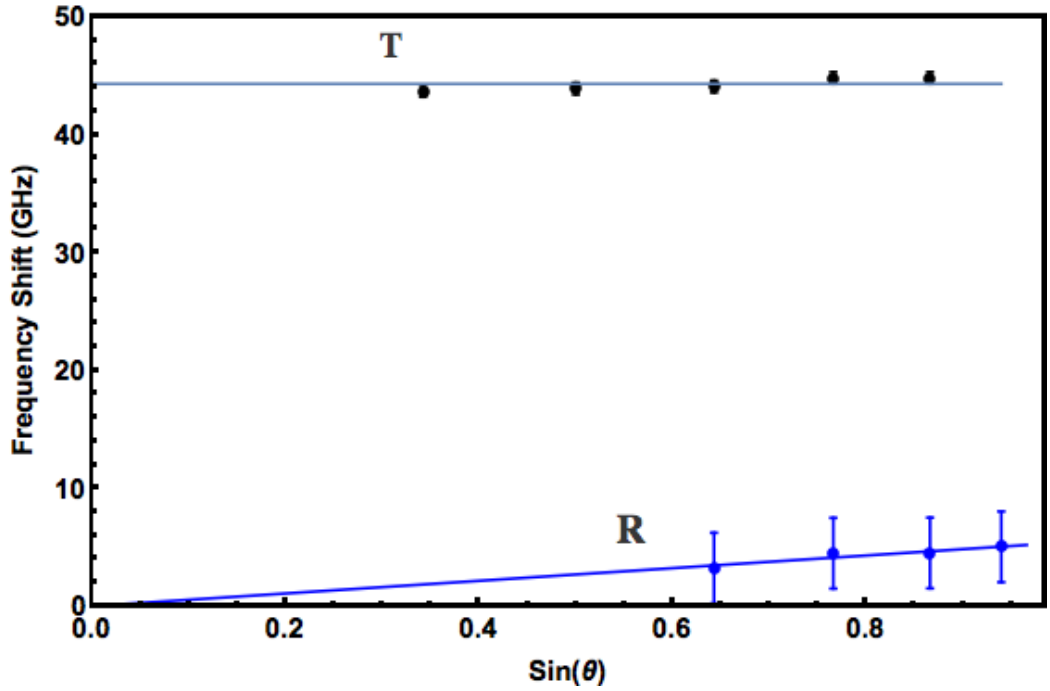

Figure 4.5: Average frequency shift versus sine of incident angle for R and T peaks in Brillouin spectrum of WS_2. The R solid line is the best fit of equation (2.23) to experimental data. The slope of the line of best fit was used to calculate the Rayleigh surface velocity for WS_2

Using equation (2.19) and knowing the refractive index of WS_2 ($n = 4.8$ at 532 nm [62]), and the frequency shift for $\theta_i = 20$, ~ 43.9 GHz, the velocity of this bulk mode was found to be $v_T = 2430 \pm 70\ m/s$. This velocity is larger than Rayleigh velocity and the frequency shift of this mode did not change with the angle of incidence. Also, this velocity is much smaller than any previously measured or calculated longitudinal velocities found in references [2] [39]. This velocity therefore is likely that of a transverse mode and it is somewhat comparable with the transverse velocity found in reference [1], ($v_T = 3500$ m).

Figure (4.5) shows the frequency shifts of the R and T peak versus the sine of the incident angle for WS_2. The frequency shift of the R peak depends linearly on $\sin\theta$ which is a characteristic of the Rayleigh surface mode. By calculating the slope of the line of best fit and using equation (2.23), the velocity of this mode was found to

be $v_R = 1430 \pm 50\ m/s$.

Elastic constant C_{44} may be estimated from the transverse phonon velocity obtained for smallest angle of incidence with respect to the z direction. The reason for that is the range of angle of incidence, 20° to 70°, results in a very small range of probed directions inside the material 3° to 9°, and these directions are close to the z-axis. Using equation (2.11), and knowing the density of WS_2 (ρ =7500 kg/m^3) [63] the C_{44} is calculated to be 44 ± 1 GPa.

4.3 Molybdenum Diselenide $MoSe_2$

Figures (4.6) show Brillouin spectra collected from samples $MoSe_2$-1 and $MoSe_2$-2, respectively. The FSR was 15 GHz, corresponding to a mirror spacing of 7.50 mm. As can be seen in both sets of spectra, a single set of Brillouin peaks was observed in nearly all spectra (labeled R) at $\theta_i \geq 30°$. The frequency shift of these peaks increases with increasing angle of incidence, which is a characteristic of the Rayleigh surface mode. The average of the frequency shift for the R peak are measured and reported in Tables (4.2) and (4.3) for $MoSe_2$-1 and $MoSe_2$-2, respectively.

The Brillouin peaks due to bulk modes are expected to appear at higher frequency shifts as mentioned before. As a result, the FSR was increased to 50 GHz, corresponding to a mirror spacing of 3 mm, as shown in Figure (4.7) for samples $MoSe_2$-1 and $MoSe_2$-2, respectively. Even with larger values of FSR, no bulk peaks were observed.

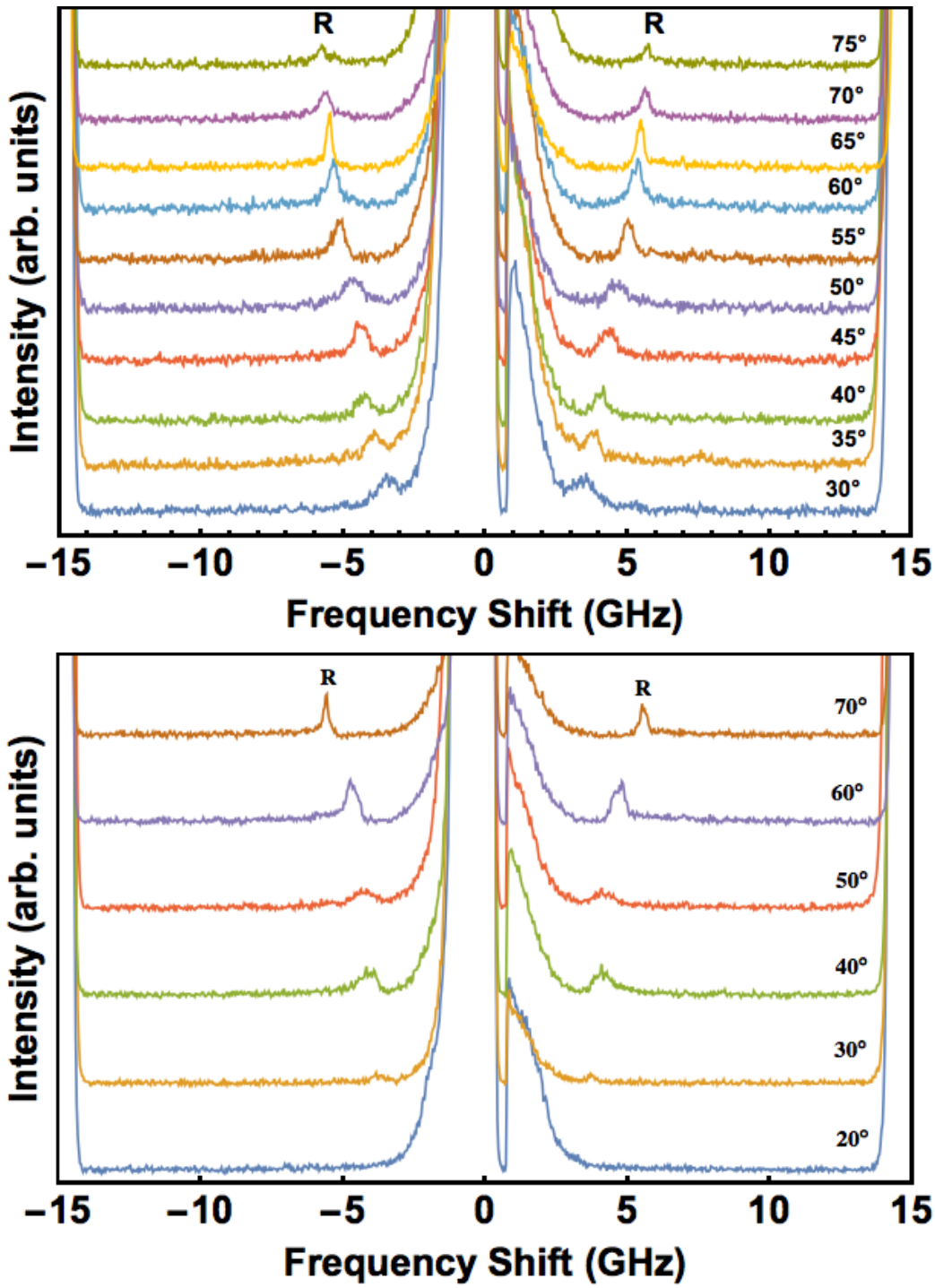

Figure 4.6: Brillouin spectra collected from $MoSe_2$-1 and $MoSe_2$-2, respectively. The free spectral range was set to 15 GHz. The numbers on the right hand side of the each spectrum indicate the incident angle.

Table 4.2: Stokes (S), anti-Stokes (AS), and average (AVE) Brillouin frequency shift for Rayleigh (R) mode peak of $MoSe_2 - 1$.

FSR	Material	Angle of Incidence ($\circ$)	f_R^S ($\pm$0.1 GHz)	f_R^{AS} ($\pm$0.1 GHz)	f_R^{AVE} ($\pm$0.1 GHz)
15	$MoSe_2$-1	75	5.7	5.8	5.7
		70	5.6	5.6	5.6
		65	5.4	5.5	5.5
		60	5.3	5.3	5.3
		55	4.9	5.2	5.1
		50	4.4	4.6	4.5
		45	4.3	4.5	4.4
		40	4.1	4.2	4.1
		35	3.7	3.9	3.5
		30	3.5	3.5	3.5
50	$MoSe_2$-1	70	5.8	5.6	5.7
		65	5.5	5.7	5.6
		60	5.5	5.5	5.5
		55	5.1	5.2	5.2
		50	4.9	5.0	4.9
		45	4.6	4.8	4.7
		40	4.1	4.0	4.1
		35	3.7	3.8	3.8

Table 4.3: Stokes (S), anti-Stokes (AS) and average (AVE) Brillouin frequency shift for Rayleigh (R) mode peak of $MoSe_2 - 2$.

FSR	Material	Angle of Incidence ($\circ$)	f_R^S ($\pm$0.1 GHz)	f_R^{AS} ($\pm$0.1 GHz)	f_R^{AVE} ($\pm$0.1 GHz)
15	$MoSe_2$-2	70	5.2	5.6	5.4
		60	4.8	4.7	4.8
		50	4.0	4.4	4.2
		40	4.0	4.0	4.0
		30	3.6	3.7	3.7
30	$MoSe_2$-2	70	5.3	5.5	5.4
		60	5.0	4.7	4.9
		50	5.0	4.7	4.9
		40	4.3	4.0	4.2
50	$MoSe_2$-2	70	5.3	5.5	5.4
		60	4.7	4.8	4.8
		50	4.3	4.1	4.2
		30	3.9	3.7	3.8

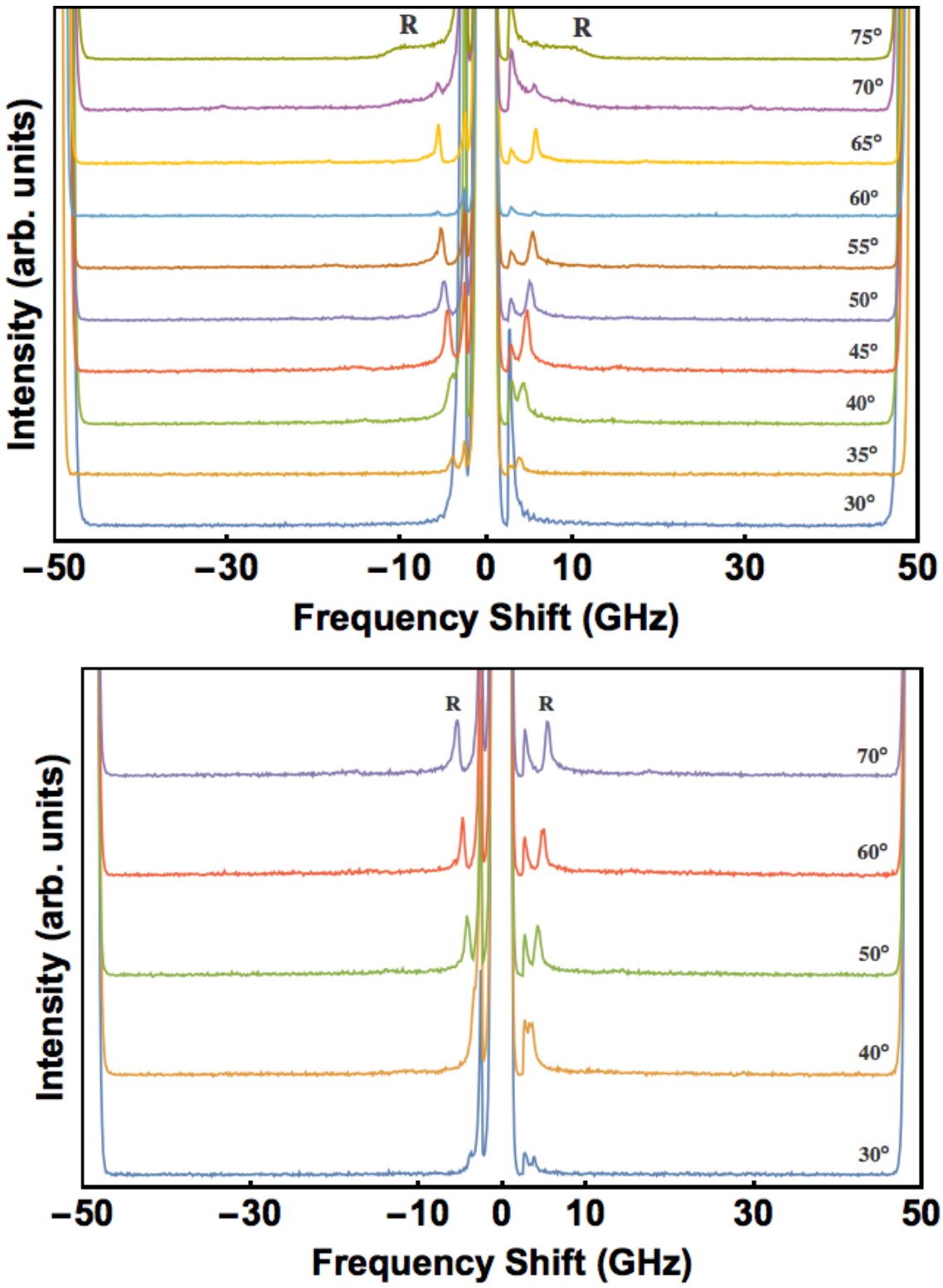

Figure 4.7: Brillouin spectra collected from $MoSe_2$-1 and $MoSe_2$-2, respectively. The free spectral range was set to 50 GHz. The numbers on the right hand side of the each spectrum indicate the incident angle.

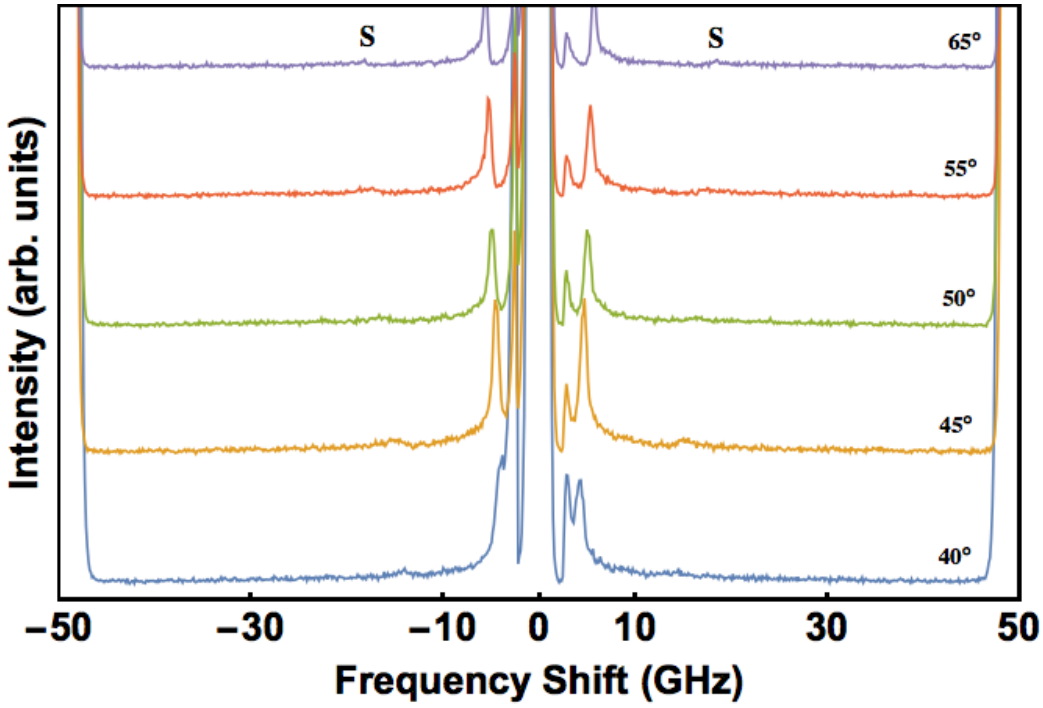

Figure 4.8: Brillouin spectra collected from $MoSe_2$-1 show Rayleigh mode peak and a second the surface related mode (S). The numbers on the right hand side of the each spectrum indicate the incident angles.

In these spectra, however, in addition to the peaks due to the Rayleigh surface mode, a second weak Brillouin doublet due to a surface-related mode was observed over a shift range ∼18-14 GHz. Also, spectra is shown in Figure (4.8), in order to more clearly show the surface related mode (labelled S). There appears to be two sets of peaks in the spectra shown in Figs. 4.7 and 4.8. The feature that looks like a peak at small frequency shifts is not really a peak at all, but is the shoulder of the central elastic peak being cut off by the shutter. The average of the frequency shift for this surface related mode were measured and are reported in Table (4.4).

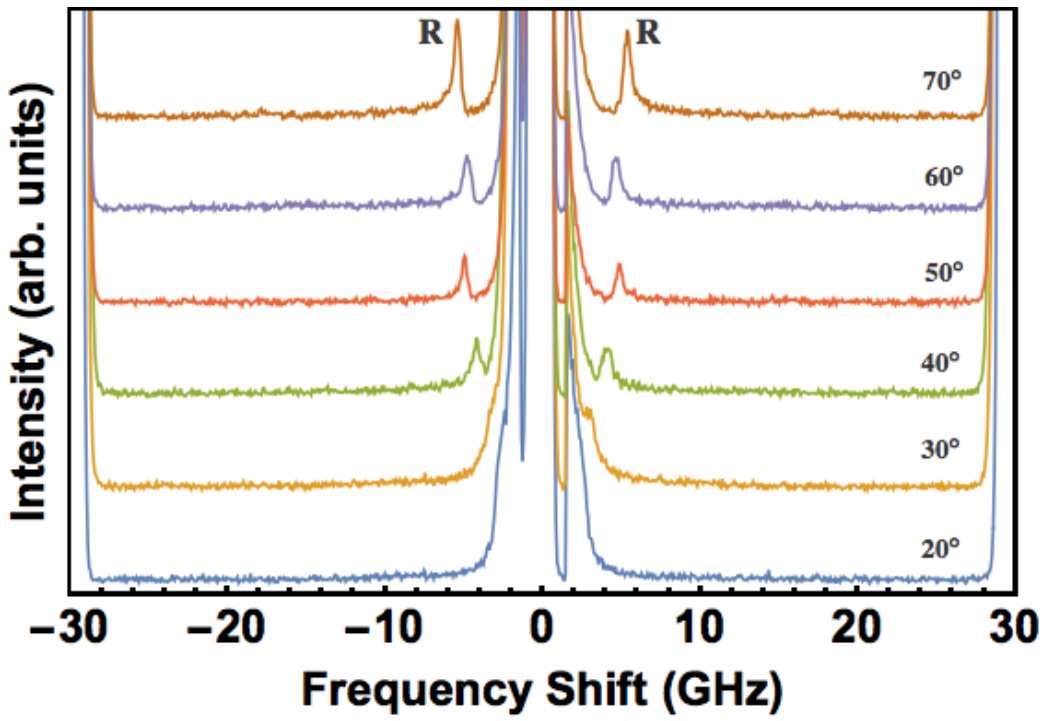

Figure 4.9: Brillouin spectra collected from $MoSe_2 - 2$. The free spectral range was set to 30 GHz. The numbers on the right hand side of the each spectrum indicate the incident angle.

Table 4.4: Stokes (S), anti-Stokes (AS) and average (AVE) Brillouin frequency shift for surface-related mode (S) of $MoSe_2 - 1$.

FSR	Material	Angle of Incidence (∘)	f_S^S (±0.1 GHz)	f_S^{AS} (±0.1 GHz)	f_S^{AVE} (±0.1 GHz)
50	$MoSe_2$-1	65	18.3	18.3	18.3
		55	17.3	17.6	17.5
		50	16.0	16.8	16.4
		45	15.3	15.7	15.5
		40	14.3	14.2	14.3

Figure (4.9) shows spectra collected from sample $MoSe_2 - 2$ at different angles of incidence from 20° to 70° with the FSR set to 30 GHz. The peaks due to the Rayleigh surface mode was observed. The frequency shift of the Rayleigh surface mode as well as a second surface-related mode increases linearly with the sine of the incident angle as shown in Figure (4.10). The velocity of surface-related mode of $MoSe_2 - 1$ was found to be 5670 m/s.

In an attempt to observe peaks due to bulk modes, spectra were collected from sample $MoSe_2$-2 at different angles of incidence from 20° to 60° with the FSR set to 150 GHz. These spectra are shown in Figure (4.11). Unfortunately, no Brillouin peaks, other than those due to the Rayleigh mode already identified, were observed in these spectra. This may be due to the fact that the extinction coefficient of $MoSe_2$ is high (about 1.9) at 532 nm [62]. Also, in the spectrum collected at $\theta_i = 30°$ there is another peak located only on one side of the central elastic peak. The fact that this peak appears on only one side of the central elastic peak indicates that it could be due to a Raman mode.

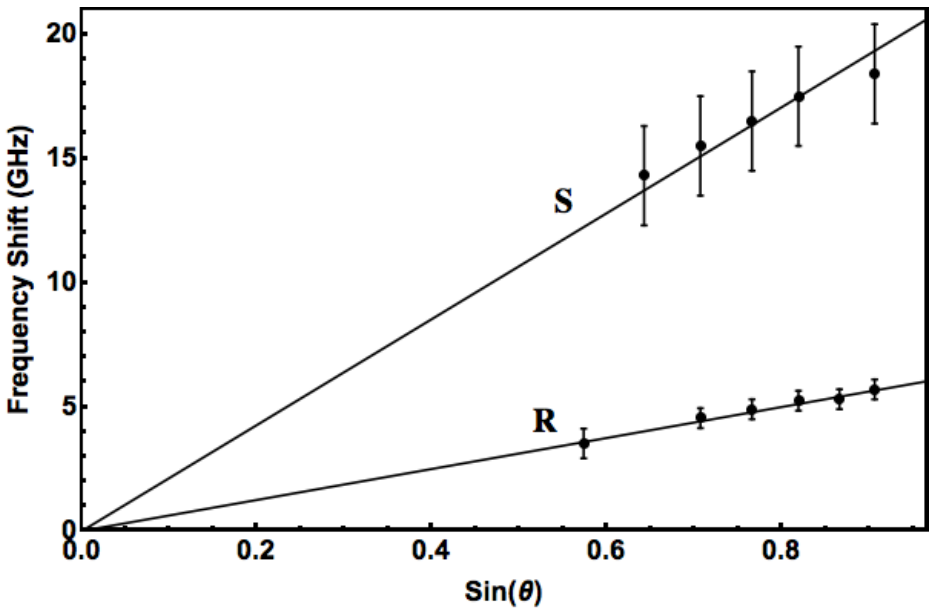

Figure 4.10: Average frequency shifts versus sine of incident angle for Rayleigh surface and surface related modes in Brillouin spectra of $MoSe_2 - 1$. The solid line is best fit of equation (2.23) to experimental data. The slope of the line of best fit was used to calculate the Rayleigh surface velocity for $MoSe_2$-1.

Using the data in Tables (4.2) and (4.3) for $MoSe_2$-1 and $MoSe_2$-2, respectively, the frequency shifts versus $\sin\theta$ were plotted and shown in Figures (4.10) and (4.12) for $MoSe_2$-1 and $MoSe_2$-2, respectively. The frequency shift of R peaks increases linearly with the sine of the incident angle. The slope of the lines of best fit was used to calculate the Rayleigh surface velocities for both samples of $MoSe_2$. The Rayleigh surface phonon velocities of the two samples of $MoSe_2$ were 1660 $\pm$ 30 m/s and 1610 $\pm$ 40 m/s, for $MoSe_2$-1 and $MoSe_2$-2, respectively. Clearly, there is good agreement between the Rayleigh surface phonon velocities for both samples.

As mentioned above, no peaks due to bulk modes were observed in the spectra of $MoSe_2$. It was therefore not possible to determine any bulk modes velocities nor elastic constants for this material.

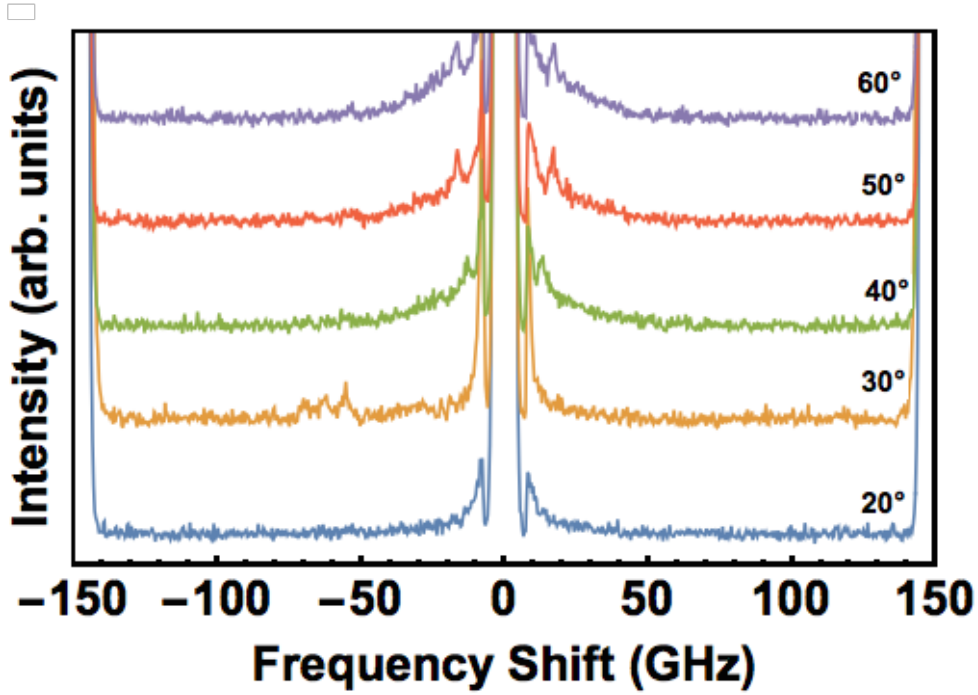

Figure 4.11: Brillouin spectra of $MoSe_2 - 2$. The free spectral range was set to 150 GHz. The numbers on the right hand side of the each spectrum indicate the incident angle.

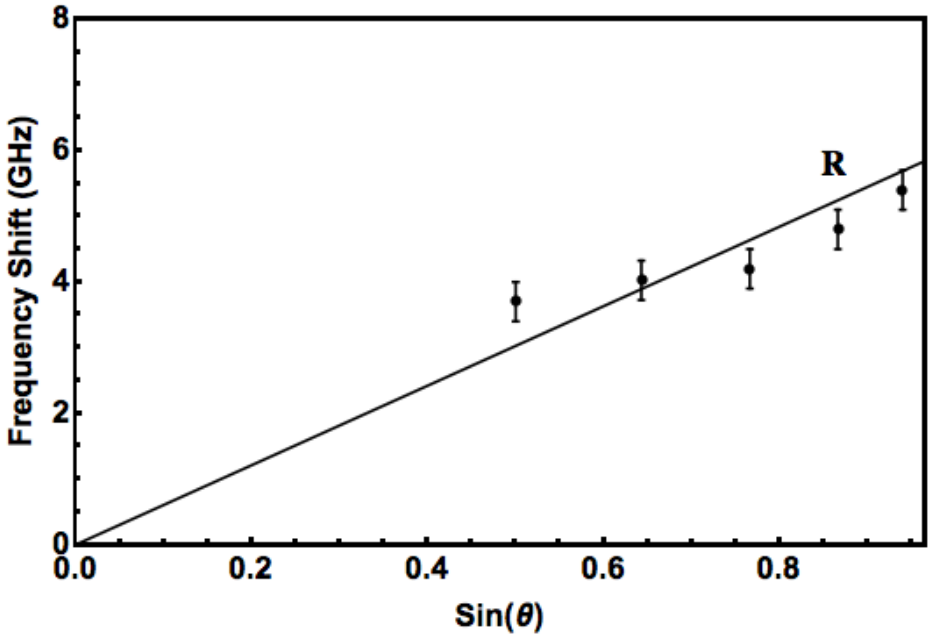

Figure 4.12: Average frequency shifts versus sine of incident angle for Rayleigh surface peaks in Brillouin spectra of $MoSe_2$-2. The solid line is best fit of equation (2.23) to experimental data. The slope of the line of best fit was used to calculate the Rayleigh surface velocity for $MoSe_2$-2.

4.4 Molybdenum Disulfide MoS_2

The Brillouin spectra collected from sample MoS_2-1 and MoS_2-2 at different angles of incidence varing from 15° to 75° with the FSR set to 15 GHz are shown in Figure (4.13). The R peak appeared at low frequency shifts and increased when the angle of incidence was increased, which is characteristic of the Rayleigh surface mode. There are no other peaks due to bulk modes in these spectra collected with the FSR set to 15 GHz. The average of the frequency shifts for the R peak were measured and are reported in Table (4.5) and (4.6) for MoS_2-1 and MoS_2-2, respectively.

Again, an attempt was made to observe peaks due to bulk modes in this material by exploring the higher frequency shift regime using an FSR of 50 GHz for both samples (see Figures 4.14). As can be seen in both sets of spectra, the R peaks were still present but no bulk modes were observed. A further attempt was made to observe peaks due to bulk modes in this material by exploring an even higher frequency shift regime using an FSR of 150 GHz but for only MoS_2-1 as shown in Figure (4.15). In these spectra, the peaks due to bulk modes were observed at frequency shift about $\sim$ 64 GHz, but they were extremely weak and wide, resulting in a large uncertainty in peak frequency shift (0.5 GHz).

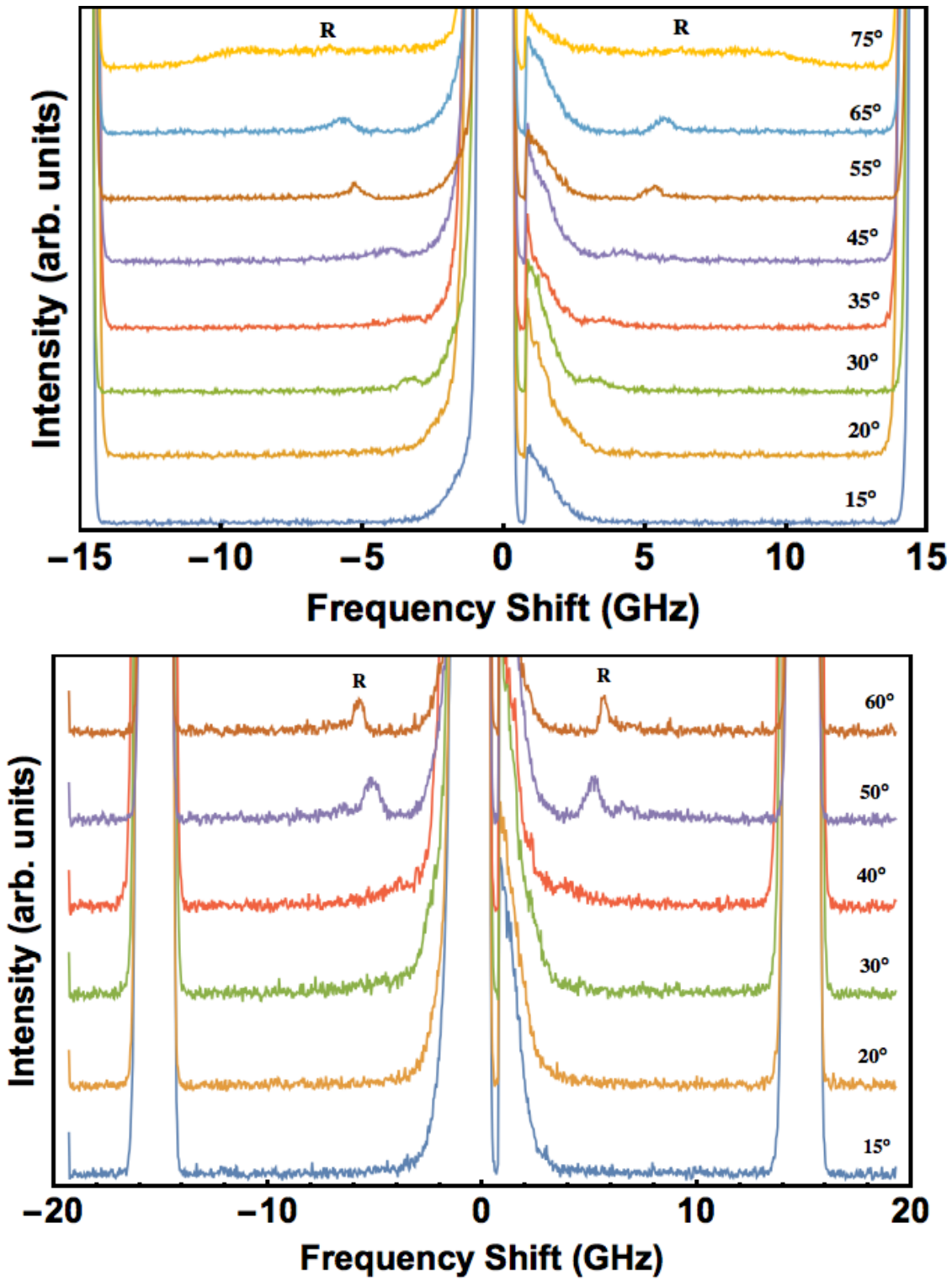

Figure 4.13: Brillouin spectra of MoS_2-1 and MoS_2-2, respectively. The free spectral range was set to 15 GHz. The numbers on the right hand side of the each spectrum indicate the incident angle.

Table 4.5: Stokes (S), anti-Stokes (AS) and average (AVE) Brillouin frequency shifts for Rayleigh (R) and transverse bulk mode (T) of $MoS_2 - 1$.

FSR	Material	Angle of Incidence (∘)	f_R^S (±0.1 GHz)	f_R^{AS} (±0.1 GHz)	f_R^{AVE} (±0.1 GHz)	f_T^S (±0.5 GHz)	f_T^{AS} (±0.5 GHz)	f_T^{AVE} (±0.5 GHz)
15	MoS_2-1	65	5.6	5.7	5.6	-	-	-
		55	5.3	5.3	5.3			
		45	4.1	4.0	4.0	-	-	-
		35	3.4	3.3	3.3	-	-	-
		30	3.1	3.3	3.2			
50	MoS_2-1	70	5.6	5.8	5.7	-	-	-
		65	5.5	5.7	5.6	-	-	-
		60	5.5	5.5	5.5	-	-	-
		50	4.6	4.8	4.7	-	-	-
		40	4.5	4.6	4.5	-	-	-
150	$MoS_2 - 1$	46	-	-	-	64.0	62.0	63.0
		15	-	-	-	64.0	64.1	64.0
		9	-	-	-	63.4	63.5	63.5

Table 4.6: Stokes (S), anti-Stokes (AS) and average (AVE) Brillouin frequency shifts for Rayleigh (R) mode peak of $MoS_2 - 2$.

FSR	Material	Angle of Incidence ($\circ$)	f_R^S ($\pm$ 0.1 GHz)	f_R^{AS} ($\pm$ 0.1 GHz)	f_R^{AVE} ($\pm$ 0.1 GHz)
15	MoS_2-2	60	5.8	5.6	5.7
		50	5.3	5.1	5.2
		40	3.8	4.1	3.9
		30	3.6	3.1	3.3
50	MoS_2-2	60	5.7	5.7	5.7
		50	5.1	5.1	5.1

Using the data in Tables (4.5) and (4.6), the frequency shift of Rayleigh surface mode versus $\sin\theta$ was plotted and is shown in Figures (4.16) and (4.17). The slopes of the lines of best fit were used to calculate the Rayleigh surface velocities for both samples of MoS_2, which are $1750 \pm 70\ m/s$ and $1630 \pm 80\ m/s$, for MoS_2-1 and MoS_2-2, respectively. As for $MoSe_2$, good agreement is obtained between the velocities for these two samples.

The frequency shift of the peaks attributed to the T mode have only a weak dependence on the angle of incidence and this is a characteristic of a bulk mode. The transverse bulk mode peaks are labeled as T. The reason for that is the range of angle of incidence, 20° to 70°, results in a very small range of probed directions inside the material 1.7° to 9° and close to the z-axis. The average of the frequency shifts for these peaks were measured and reported in Table (4.5) and (4.6). Also, bulk velocities was calculated by using Equation (2.19) and knowing the refractive index ($n = 4.9$ at 532 nm [64]), which is $3450 \pm 100\ m/s$. Finally, it should be noted that some peaks in these spectra are so weak that a reliable frequency shift value could not be obtained.

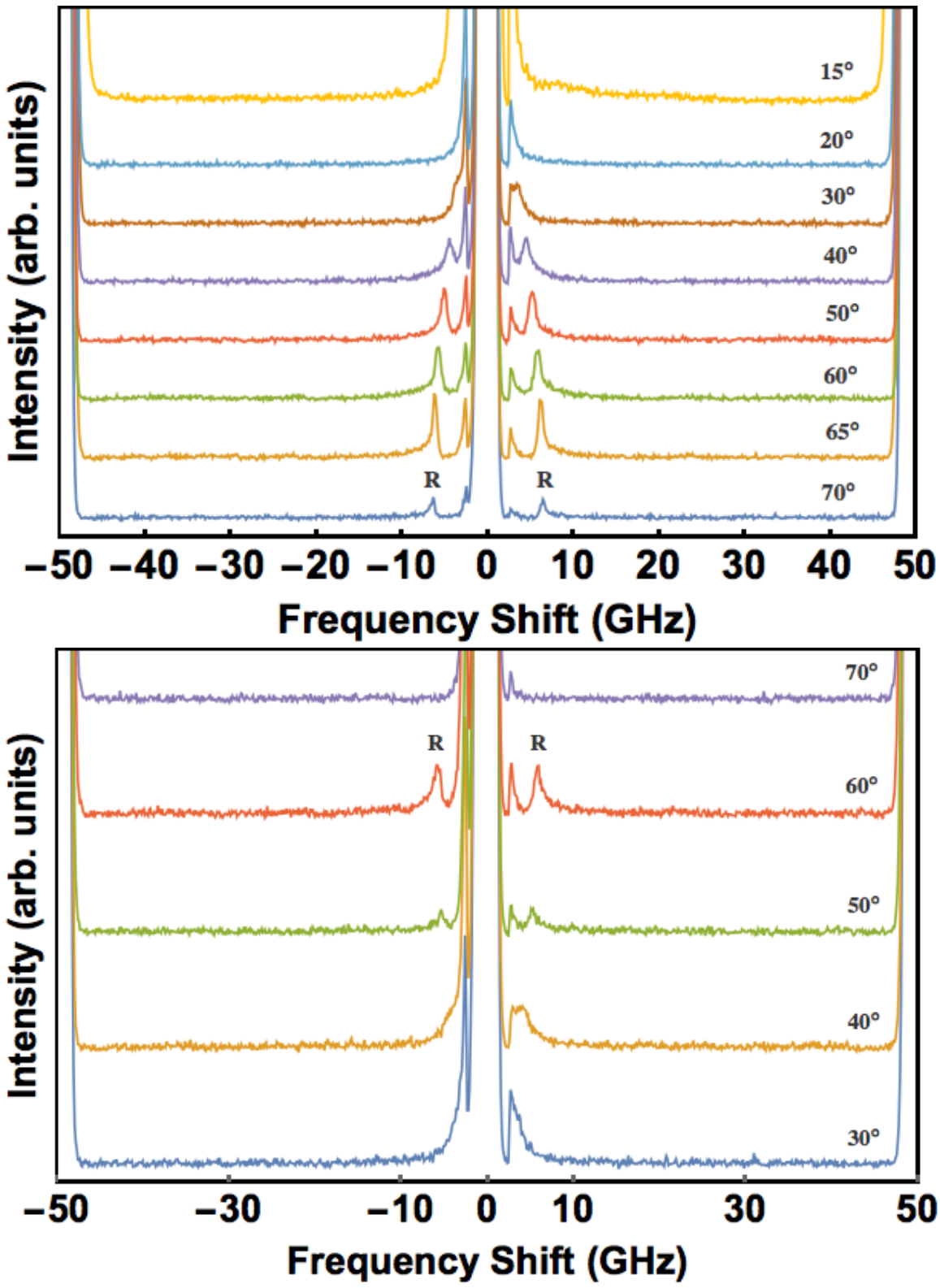

Figure 4.14: Brillouin spectra collected from MoS_2-1 and MoS_2-2, respectively, at various angles of incidence. The free spectral range was set to 50 GHz. The numbers on the right hand side of the each spectrum indicate the incident angles.

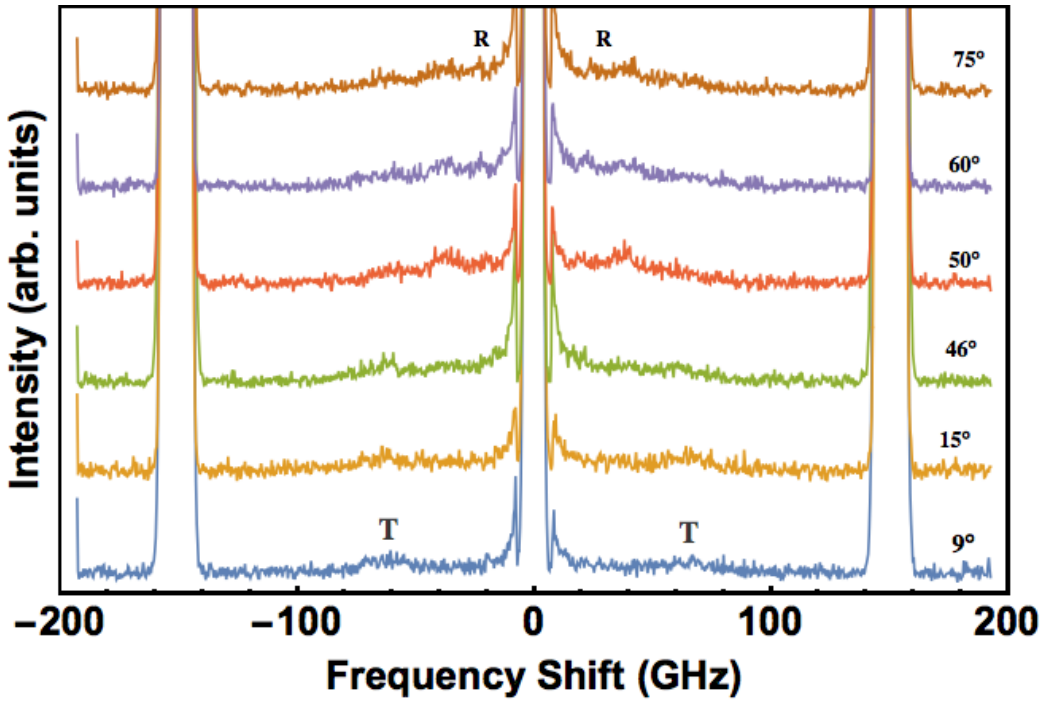

Figure 4.15: Brillouin spectra collected from MoS_2-1 at various angles of incidence. The free spectral range was set to 150 GHz. The numbers on the right hand side of the each spectrum indicate the incident angles.

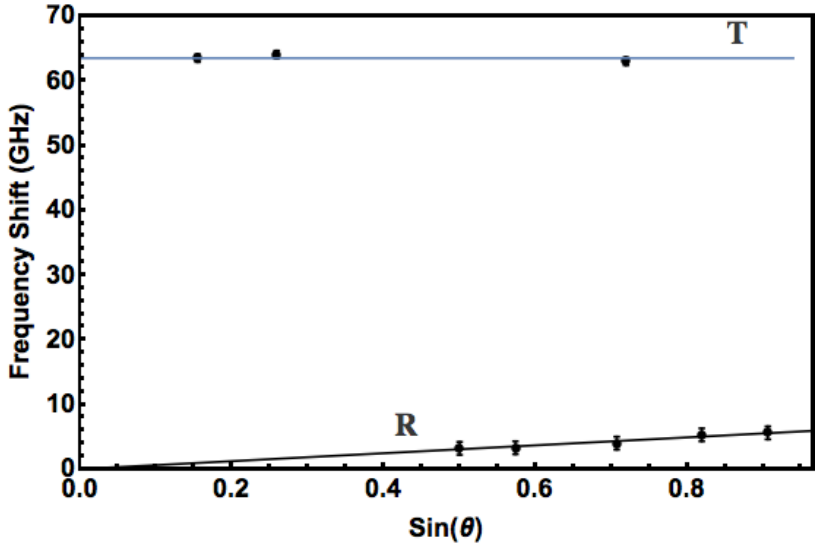

Figure 4.16: Average frequency shift versus sine of incident angle for R and T peaks in Brillouin spectra of MoS_2-1. The R solid line is best fit of equation (2.23) to experimental data. The slope of the line of best fit was used to calculate the Rayleigh surface velocity for MoS_2-1

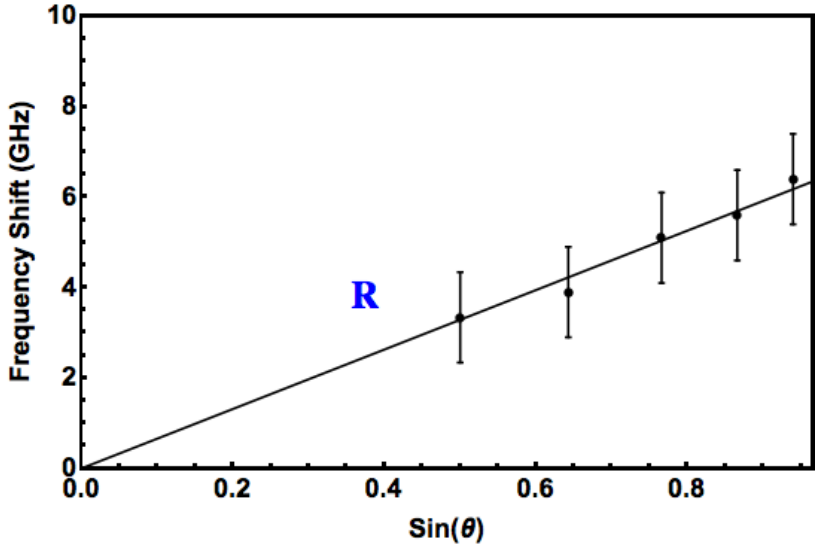

Figure 4.17: Average frequency shift versus sine of incident angle for R peaks in Brillouin spectra of MoS_2-2. The R solid line is best fit of equation (2.23) to experimental data. The slope of the line of best fit was used to calculate the Rayleigh surface velocity for MoS_2-2

Elastic constant C_{44} may be estimated from the transverse phonon velocity obtained for smallest angle of incidence. Since the range of angles used here was from 20° to 70°, the range of directions probed inside the material was found by Snell's law to be from 1.7° to 9°. Using equation (2.11), and knowing the density of MoS_2 ($\rho = 5060\ kg/m^3$ [63]), C_{44} was calculated to be 60 ± 3 GPa.

4.5 Discussion

In all spectra of three different materials the Rayleigh surface modes were observed while the bulk transverse modes were only seen in WS_2 and MoS_2. Table (4.7) presents the extinction coefficients and optical penetration depth for these three materials. The extinction coefficients were caculated using the equation [65] $\mathrm{k} = \left(\frac{\sqrt{\epsilon_1^2+\epsilon_2^2}-\epsilon_1}{2}\right)^{1/2}$ where ε_1, and ε_2 are dielectric constants estimated from reflectivity spectra in reference [62]. The penetration depth is calculated from $\mathrm{d} = \frac{1}{\alpha} = \frac{\lambda}{4\pi k}$ where d, α, λ and k are penetration depth, absorption coefficient, wavelength, and extinction coefficient, respectively. As can be seen in the table (4.7), the extinction coefficient for $MoSe_2$ is much larger than those for WS_2 and MoS_2. This could be the reason why no bulk mode was observed in the Brillouin spectra of $MoSe_2$. It is obvious that due to smaller penetration depth for $MoSe_2$ in comparison with WS_2 and MoS_2, not much light is able to penetrate into the bulk of this material and thus the scattering volume would be largely confined to the surface. Surprisingly, peaks due to bulk modes were also not observed in BLS experiment on WSe_2 [29] even though the optical penetration depth is slightly larger than that for MoS_2.

Table 4.7: Extinction coefficients of WS_2, MoS_2 and $MoSe_2$ at 532 nm.

Material	Extinction Coefficient	Reference	Bulk Mode Present in Spectra?	Optical Penetration Depth (nm)
WS_2	0.62	[Present work]	Yes	86
MoS_2	1.12	[Present work]	Yes	37
$MoSe_2$	1.95	[Present work]	No	21
WSe_2	1.0	[29]	No	42

Table 4.8: Acoustic phonon velocities of WS_2, MoS_2 and $MoSe_2$ determined in the present work and previous studies.

Material	Technique	Sample Type	v_R (m/s)	v_T (m/s)	v_L (m/s)
WS_2	Brillouin Scattering [Present work]	Bulk- 2H-WS_2	1430 ± 50	2430 ± 70	-
	First Principles Calculation [1]	Single Layer	-	3500	5500
	First Principles Calculation [2]	Single Layer	-	-	4300
	Full-Potential Local-Orbital Code [39]	Bulk- 2H-WS_2	-	-	6670
MoS_2	Brillouin Scattering [Present work]	Bulk- 2H-MoS_2	1690 ± 80	3450 ± 100	-
	First Principles Calculation [1]	Single Layer	-	4100	6400
	First Principles Calculation [4]	Single Layer	-	4200	6700
	Full-Potential Local-Orbital Code [39]	Bulk- 2H-MoS_2	-	-	7930
	First Principles Calculation [2]	Single Layer	-	-	6600
$MoSe_2$	Brillouin Scattering [Present work]	Bulk- 2H-$MoSe_2$	1630 ± 40	-	-
	First Principles Calculation [1]	Single Layer	-	3000	6800
	Full-Potential Local-Orbital Code [39]	Bulk- 2H-$MoSe_2$	-	-	6010
	First Principles Calculation [2]	Single Layer	-	-	4100
	First Principles Calculation [3]	Single Layer	-	900	1500
$NbSe_2$	Brillouin Scattering [44]	Layered	1571	-	-
TaS_2	Brillouin Scattering [44]	Layered	1220	-	-
WSe_2	Brillouin Scattering [29]	Bulk- 2H-WSe_2	1340 ± 20	-	-

4.5.1 Acoustic Phonon Velocities

Table (4.8) shows the Rayleigh surface phonon velocities and the transverse acoustic phonon velocities approximately along the z direction for all materials from the current study. As can be seen, the Rayleigh surface velocity of $MoSe_2$ is 12% higher than that for WS_2 and also 3% lower than that for MoS_2. Moreover, the Rayleigh surface velocity of MoS_2 is higher than WS_2. Due to the absence of related theoretical and experimental studies of the Rayleigh surface velocity of $MoSe_2$, $MoSe_2$, and WS_2 it was not possible to compare our calculated Rayleigh surface phonon velocities with other results. However, we compared our results of the Rayleigh surface velocity with other transition metal dichalcogenides in Table (4.8). The study reported by Harley and Fleury [44] conducted Brillouin scattering to investigate the velocities of surface and bulk acoustic waves in 2H-$NbSe_2$ and TaS_2 at room temperature in a backscattering geometry. As can be seen, the Rayleigh surface velocity of $MoSe_2$ obtained in this work is similar (within 3%) to the Rayleigh surface velocity of $2H-NbSe_2$ in reference [44]. Also, the Rayleigh surface velocity of WS_2 is similar with the study reported by Akintola *et al.* [29] on Brillouin Scattering study of WSe_2 obtained at room temperature in a backscattering geometry, the difference being 6 %.

Table (4.8) also presents bulk acoustic phonon velocities approximately along the z direction determined in the present work and in previous studies. As mentioned, no peaks due to longitudinal bulk modes were observed in any of the collected spectra in this study. Transverse bulk mode peaks were observed for WS_2 and one sample of MoS_2, but were not seen in spectra collected from either sample of $MoSe_2$. As can be seen, the transverse bulk velocity of MoS_2, 3450 $\pm$ 100 m/s, is higher than that of WS_2, 2430 $\pm$ 70 m/s. Due to the difference in atomic mass and bonding stiffness the three acoustic branches of MoS_2 are higher than WS_2. As a result, the group velocity of acoustic phonons in MoS_2 are larger than WS_2 [1] (the direction of phonon

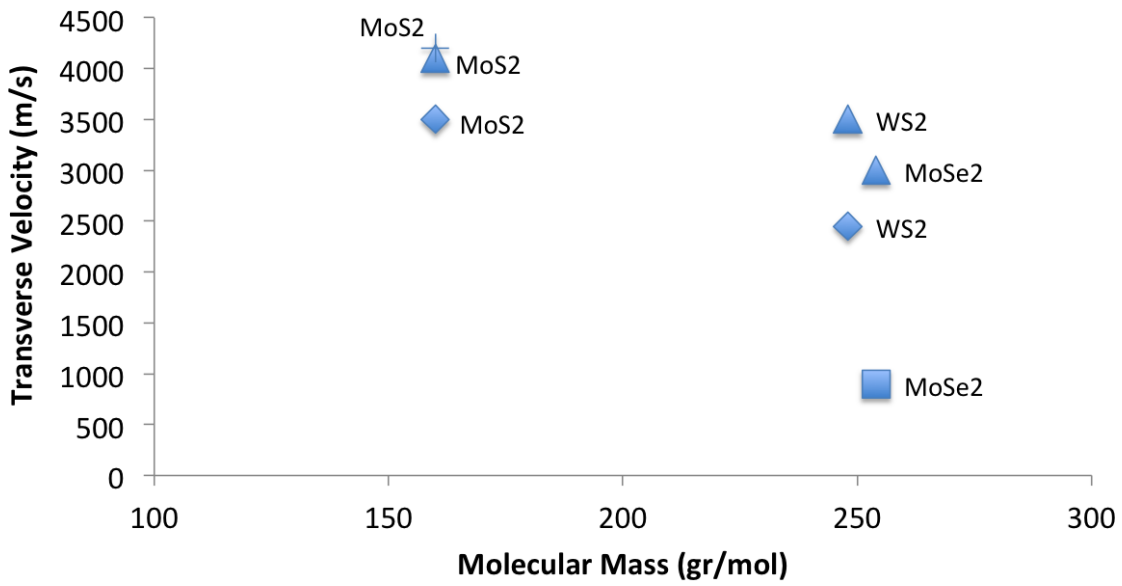

Figure 4.18: The transverse bulk acoustic phonon velocity of all materials mentioned in Table (4.8) versus the molecular mass. △- ref [1],○-ref [2], □ -ref [3] and + -ref [4] and ◇ - present work.

propagation is not presented in this ref [1]). Figure (4.18) shows the transverse bulk acoustic phonon velocities of some of materials in Table (4.8) versus the molecular mass. There is no obvious trend. Also, the results of the present work show a decrease in velocity with increasing metal row number in the Periodic Table which is not consistent with the results in reference [27].

Fortunately, in some theoretical works the transverse bulk acoustic phonon velocities have been calculated and so one can compare our results with previous studies. The transverse velocity of WS_2 obtained in this work shows a 44% difference from the value given in reference [1], 3500 m/s. Also, the transverse velocity of MoS_2 is in a reasonable agreement with in-plane transverse velocity measurements by Gu *et al.* [1] and Kaasbjerg *et al.* [4] (16 % and 19 %, respectively). The diference could arise from the single layer of TMDCs material which they used in their study. Also, Harley and Fleury [44], observed a weak bulk mode with velocity 5000 m/s in 2H-$NbSe_2$ and

TaS_2. As been discussed no bulk mode was observed in either Brillouin spectra of sample of $MoSe_2$ in this study.

4.5.2 Elastic constant C_{44}

Table (4.9) presents elastic constant C_{44} for WS_2 and MoS_2. This table also shows some results from other theoretical and experimental studies. In this work the value of C_{44} for WS_2 was determined to be 44 ± 1 GPa. This value is considerably different from that obtained by Raman scattering [66] (16 GPa) and also from first principles calculation [34] (58.63GPa). It is likely that the reason for this large difference between these studies and the present work is that the former were carried out on single layer WS_2. A first principles study done on bulk WS_2 [35] also shows a relatively large difference with the current results ($C_{44} = 25$ GPa). The reason for this is not clear.

The value of the elastic constant C_{44} is 60 ± 3 GPa for MoS_2. The current elastic constant value is consistent with the calculated value obtained value in reference [34] (51.43 GPa). This is somewhat surprising become the first principles calculation of reference [34] were done for a single layer sample of this material. It is worth noting, however, that the value of C_{44} obtained for WS_2 from reference [34] also shows the best agreement with the present work. There is a big difference, however, between the current results and that of reference [33] (18 GPa) and experimentally using neutron scattering [41], (19 GPa), even though bulk samples of 2H-MoS_2 were used. Another theoretical study [32] reported $C_{44} = 30$ GPa for a bulk sample which is about half of the value obtained in the present work. A theoretical study done by Valentin *et al.* [36] used the periodic Hartree-Fock method with different degrees of freedom. Each degree of freedom results in a different value of C_{44}. The values obtained were 9.11 GPa, 8.74 GPa, and 14.89 GPa. All these values are much smaller than the value obtained in the current study. The difference could be explained by the different

number of layers, six or eight layers, used in that study which cannot be considered as a bulk material. Another theoretical study [37] used the periodic Hartree-Fock and two DFT different pseudo-potential methods to calculate C_{44} of MoS_2. They found that C_{44} is 30 GPa, 26 GPa, and 19 GPa for Hartree-Fock and two DFT pseudo-potential methods, respectively. The calculations performed in this study where done on few-layer MoS_2 (4, 6, 8 layers) not bulk MoS_2, which could again account for the difference between these results and current study. The last two references, [36] and [37], did not include the van-der Waalls interactions in their calculations, so that could be one reason for observed discrepancy. Also, the results of the present work show MoS_2 has greater elastic constant value than the elastic constant value of WS_2 which is not consistent with the results in reference [34].

As stated earlier, Brillouin peaks due to bulk modes were not seen for either sample of $MoSe_2$ so it was not possible to obtain the bulk velocities and elastic constants for this material.

Table 4.9: Elastic constant C_{44} of WS_2 and MoS_2 from current work and previous studies.

Material	Technique Used and Reference	Sample Type	C_{44} (GPa)	Difference %
WS_2	Brillouin Scattering [Present Work]	Bulk- 2H-WS_2	44 ± 1	-
	First Principles Calculation [34]	Single Layer	58.63	33
	First Principles Calculation [35]	Bulk- 2H-WS_2	25	43
	Raman Scattering [66]	Single Layer	16	63
MoS_2	Brillouin Scattering [Present Work]	Bulk- 2H-MoS_2	60 ± 3	-
	First Principles Calculation [34]	Single Layer	51.43	14
	Hybrid-DFT [33]	Bulk- 2H-MoS_2	18	70
	First Principles Calculation [32]	Bulk- 2H-MoS_2	30.043	49
	Neutron Scattering [41]	Bulk- 2H-MoS_2	19	68
	Periodic Hartree-Fock Methods [36]	Few-layer (4, 6, 8)	9.11, 8.74, 14.89	84, 85, 75
	Periodic Hartree-Fock and DFT Methods [37]	Few-layer (4, 6, 8)	30, 26,19	50, 56, 68

Chapter 5

Conclusions

In this work, Brillouin light scattering spectroscopy has been used for the first time to study surface and bulk acoustic modes of the transition metal dichalcogenides MoS_2, $MoSe_2$, and WS_2. Rayleigh surface and transverse bulk acoustic phonon velocities were obtained from the frequency shifts of peaks observed in the Brillouin spectra. Rayleigh velocities were calculated to be 1690 $\pm$70 m/s, 1630 $\pm$40 m/s, and 1430 $\pm$50 m/s for MoS_2, $MoSe_2$, and WS_2, respectively. These are the first measurements of Rayleigh surface phonon velocities in these materials. Peaks due to transverse bulk acoustic modes were only observed for WS_2 and MoS_2 at frequency shifts of $\sim$ 43 and $\sim$ 62 GHz, respectively. The corresponding velocities approximately along z crystallographic axis were found to be 2430 $\pm$ 70 m/s and 3450 $\pm$ 100 m/s for WS_2 and MoS_2, respectively. These velocities were compared to those obtained in previous studies [1] and [4] (21%, and 44% for MoS_2, and WS_2, respectively). From the transverse acoustic phonon velocities for WS_2, and MoS_2, elastic constant C_{44} was determined to be 44 $\pm$ 1 GPa, and 60 $\pm$ 3 GPa, respectively. These values were compared with first-principles calculations [32, 34, 35], Hybrid-DFT [33], and Raman scattering measurements [66]. References [34] and [66] were done on single layer

samples and therefore cannot be directly compared with the results of the present work on bulk crystals of these materials. However, the results from [32,33,35] and [41] also, showed discrepancies although bulk sample were used. The reason for this difference is not clear. The references, [36] and [37], did not include the van-der Walls interactions in their calculations, so that could be one reason for obsreved discrepancy.

The results obtained in this work can be used to investigate the reliability and accuracy of theoretical models and other experimental approaches for determination of elastic properties of TMDCs. Understanding of acoustic wave propagation and the mechanical properties of transition metal dichalcogenides are important for future use of them in optoelectronic and acousto-optic device applications.

Future work could using Brillouin studies with different scattering geometry. This would help the remaining elastic constants of these materials to be determined.

Bibliography

[1] X. Gu and R. Yang. *Appl. Phys. Lett.*, **105**:131903, (2014).

[2] Z. Jin, X. Li, J. Mullen, and K. Kim. *Phys. Rev. B*, **90**:045422, (2014).

[3] S. Horzum, H. Sahin, S. Cahangirov, P. Cudazzo, A. Rubio, T. Serin, and F. M. Peeters. *Phys. Rev. B*, **87**:125415, (2013).

[4] K. Kaasbjerg, K. S. Thygesen, and K. W. Jacobsen. *Phys. Rev. B*, **85**:115317, (2012).

[5] V. Sorkin, H. Pan, H. Shi, S. Y. Quek, and Y. W. Zhang. *Taylor and Francis Group*, **39**:321, (2014).

[6] S. K. Srivastava and B. N. Avasthi. *J. Mater. Sci.*, **20**:3801–3815, (1985).

[7] W. S. Yun, S. W. Han, S. C. Hong, I. G. Kim, and J. D. Lee. *Phys. Rev. B.*, **85**:033305–1, (2012).

[8] Q. H. Wang, K. Kalantar-Zadeh, A. Kis, J. N. Coleman, and M. S. Strano. *Nat. Nanotechnol.*, **7**:699–711, (2012).

[9] H. Zhao, F. Xia Q. Guo, and H. Wang. *Nanophotonics*, **4**:128–142, (2015).

[10] A. K. Geim and K. S. Novoselov. *Nat. Mater.*, **6**:183–191, (2007).

[11] B. K. Ridley. *J. Phys.*, **15**:5899, (1982).

[12] D. J. Late, C. S.Rout, D. Chakravarty, and S. Ratha. *Can. Chem. Trans*, **3**:118–157, (2015).

[13] K. F. Mak, C. Lee, J. Hone, J. Shan, and T. F. Heinz. *Phys. Rev. Lett.*, **105**, (2010).

[14] Z. M. Wang. *MoS_2 Materials, Physics, and Devices.* Springer International Publishing Switzerland, 2014.

[15] A. Enyashin, L. Yadgarov, L. Houben, I. Popov, M. Weidenbach, R. Tenne, M. Bar-Sadan, and G. Seifert. *J. Phys. Chem.*, **115**:24586–24591, (2011).

[16] L. Houben, A. N. Enyashin, Y. Feldman, R. Rosentsveig, D. G. Sttoppa, and M. Bar-Sadan. *J. Phys. Chem.*, **3**:24350–24357, (2012).

[17] R. Mao, B. D. Kong, and K. W. Kim. *J. Appl. Phys.*, **116**:034302, (2014).

[18] P. P. Hankare, P. A. Chate, S. D. Delekar, V. M. Bhuse, M. R. Asabe, B. V. Jadhav, and K. M. Garadkar. *J. Cryst. Growth*, **291**:40–44, (2006).

[19] P. Tonndorf, R. Schmidt, P. Bóttger, X. Zhang, J. Bórner, A. Liebig, M. Albrecht, C. Kloc, O. Gordan, D. R. T. Zahn, S. Vasconcellos, and R. Bratschitsch. *Opt. Express*, **21**:4908–4916, (2013).

[20] S. Xu, X. Gao, J. Sun, M. Hu, D. Wang, D. Jiang, F. Zhou, L. Weng, and W. Liu. *J. Coating. Tech.*, **247**:30–38, (2014).

[21] T. Georgiou, H. Yang, R. Jalil, J. Chapman, K. Novoselova, and A. Mishchenko. *Dalton Trans*, **43**:10388–10391, (2014).

[22] P. P. Hankare, A. H. Manikshete, D. J. Sathe, P. A. Chate, A. A. Patil, and K. M. Garadkar. *JAllC*, **479**:657–660, (2009).

[23] W. Yongsheng C. Qiannan F. Ceballos J. He, D. He and Z. Hui. *Nanoscale*, **7**:9526–9531, (2015).

[24] R. Ganatra and Q. Zhang. *ACS Nano*, **8**:4074–4099, (2014).

[25] R. C. Cooper, L. Changgu, C. A. Marianetti, W. Xiaoding, H. James, and J. W. Kysar. *Phys. Rev. B*, **87**:035423, (2013).

[26] K. A. N. Duerloo, M. T. Ong, and E. J. Reed. *J. Phys. Chem. Lett.*, **3**:2871–2876, (2012).

[27] D. Çakır, M. P. Francois, and S. Cem. *Appl. Phys. Lett.*, **104**:203110., (2014).

[28] S. Roth M. S. Skolnick and H. Alms. *Phys. Stat. Sol.*, **10**:2523, (1977).

[29] K. Akintola, G. T. Andrews , SH. Curnoe, MR. Koehler, and V. Keppens. *J. Phys. Condens. Matter*, **27**:395401, (2015).

[30] N. Tunghthaithip, T. Bovornatanaraks, and N. Phaisangittisakul. *TJP*, **10**:17002, (2014).

[31] A. Kumar and PK. Ahluwalia. *Mater. Chem. Phys.*, **135**:755–761, (2012).

[32] W. Li, J. Chen, Q. He, and T. Wang. *Physica B: Condens. Matter*, **405**:2498–2502, (2010).

[33] H. Peelaers and C. G. Van de Walle. *J. Phys. Chem. C*, **118**:12073–12076, (2014).

[34] F. Zeng, W. Zhang, and B. Tang. *arXiv*, **1**:1505–1640, (2015).

[35] F. Li-ping, W. Zhi-Qiang, and Liu. Zheng-Tang. *Solid State Commun*, **187**:43 – 47, (2014).

[36] V. Alexiev, R. Prins, and T. Weber. *Phys. Chem. Chem. Phys.*, **2**:1815–1827, (2000).

[37] T. Todorova, V. Alexiev, R. Prins, and T. Weber. *Phys. Chem. Chem. Phys.*, **6**:3023–3030, (2004).

[38] C. Muratore, V. Varshney, J. J. Gengler, J. J. Hu, J. E. Bultman, T. M. Smith, P. J. Shamberger, B. Qiu, X. Ruan, A. K. Roy, and A. A. Voevodin. *Appl. Phys. Lett.*, **102**, (2013).

[39] W. Zhang, Z. Huang, W. Zhang, and Y. Li. *Nano Research*, **7**:1731–1737, (2014).

[40] S. Bertolazzi, J. Brivio, and A. Kis. *ACS Nano*, **5**:9703–9709, (2011).

[41] J. L. Feldman. *J. Phys. Chem. Solids*, **37**:1141–1144, (1976).

[42] S. V. Bhatt, MP. Deshpande, V. Sathe, R. Rao, and RH. Chaki. *J. Raman Spectrosc.*, **45**:971–979, (2014).

[43] JM. Karanlikas, R. Sooryakumar, C. Carlone, and M Aubin. *Rhys. Rev. B*, **41**:1516, (1990).

[44] R. T. Harley and P. A. Fleury. *J. Phys. C: Solid State Phys*, **12**:L863, (1979).

[45] L. Xiao and Z. Hongwei. *J Materiomics*, **1**:33–44, (2015).

[46] J. Pu, L. J. Li, and T. Takenobu. *Phys. Chem.*, **16**:14996–15006, (2014).

[47] H. Wang, F. Hongbin, and Li. Jinghong. *Small*, **10**:2165–2181, (2014).

[48] D. Jariwala, V. K. Sangwan, L. J. Lauhon, T. J. Marks, and M. C.Hersam. *ACS Nano*, **8**:1102–1120, (2014).

[49] K. Chang and W. Chen. *ACS Nano*, **5**:4720–4728, (2011).

[50] Q. H. Wang, K. Kalantar-Zadeh, A. Kis, J. N.Coleman, and M. S.Strano. *Nat. Nanotechnol*, **7**:699–712, (2012).

[51] L. D. landau and E. M. Lifshitz. *Theory of Elasticity*. Elesvier, New York , 1986.

[52] Auld and B. Alexander. *Acoustic Fields and Waves in Solids*. Melbourne, FL: Krieger, (1990).

[53] E. Robert Newnham. *Properties of Materials: Anisotropy, Symmetry, Structure: Anisotropy, Symmetry, Structure*. OUP Oxford, 2004.

[54] T. Still. *High Frequency Acoustics in Colloid-Based Meso and Nanostructures by Spontaneous Brillouin Light Scattering*. Springer Science and Business Media, Germany 2010.

[55] M. A. Omar. *Elementary Solid State Physics*. Pearson Education India, 1975.

[56] M. Cardona and R. Merlin. *Light Scattering in Solids*. Springer, US 2007.

[57] W. Hayes and R. Loudon. *Scattering of Light by Crystals*. Courier Corporation, 2012.

[58] R. Loudon and J. R. Sandercock. *J. Phys. C*, **13**:2609–22, (1980).

[59] J. R. Sanderocock. *Solid State Commun.*, **26**(8):547 – 551, (1978).

[60] B. E. A. Saleh and M. C. Teich. *Fundamentals of Photonics*. New York Wiley, 1991.

[61] Z. Mutlu, D. Wickramaratne, H. H. Bay, Z. J. Favors, M. Ozkan, R. Lake, and C. S. Ozkan. *Phys. Status Solidi A*, **211**:2671–2676, (2014).

[62] A R. Beal and H P. Hughes. *Phys. Stat. Sol.*, **12**:881, (1979).

[63] B. A. Baumgarten and D. S. Tordonato. *Materials Engineering and Research Laboratory, Technical Service Center*, **86**:8–14, (2011).

[64] Y. Li, A. Chernikov, X. Zhang, A. Rigosi, M. Hill, A. van der Zande, C. Daniel, E. Shih, J. Hone, and T. Heinz. *Phys. Rev. B*, **90**:205422, (2014).

[65] W. Frederick. *Optical Properties of Solids*. Academic Press, New York, 1972.

[66] M. Fouassier C. Sourisseau, F. Cruege and M. Alba. *J. Chem. Phys*, **150**:281–293, (1991).